POLITECNICO DI MILANO

Scuola di Ingegneria Industriale e dell'Informazione

Corso di Laurea Magistrale in Ingegneria Fisica

Dipartimento di Fisica

X-ray Raman Spectroscopy on Iridate Perovskites

Relatore
Prof. Giacomo **Ghiringhelli**

Tesi di Laurea di
Matteo **Rossi**
matr. 787488

Correlatori
Dott. Marco **Moretti**
Dott. Michael **Krisch**

Anno Accademico 2013/2014

"The process of scientific discovery is,
in effect, a continual flight from wonder."

A. Einstein

Abstract

In this thesis a X-ray Raman scattering study of the electronic structure of the first two compounds of the Ruddlesden-Popper series $Sr_{n+1}Ir_nO_{3n+1}$ ($n = 1, 2$) of iridates is presented. The measurements were performed at beam line ID20 at the European Synchrotron Radiation Facility, Grenoble.

$5d$ transition metal oxides, iridates in particular, have recently been intensively explored as they display new fascinating phenomena, arising from the strong spin-orbit coupling to which they are subjected. Indeed, a simple Hubbard model, applied with great success to $3d$ transition metal oxides, would predict a metallic state for these $5d$ compounds, in view of the larger bandwidth and smaller electron correlation in the $5d$ orbitals; instead, some iridates, among which the samples studied, are insulators. The opening of a gap is due to the strong spin-orbit coupling which enhances the effect of correlation, narrows the effective bandwidth and isolates the so-called $J_{\text{eff}} = 1/2$ ground state. This peculiar ground state is strictly achieved only if the energies at play, most especially the cubic and tetragonal components of the crystal field splitting and the spin-orbit coupling, follow a precise hierarchy.

The aim of this work is to determine the cubic crystal field splitting of the Ir $5d$ states in Sr_2IrO_4 and $Sr_3Ir_2O_7$ by X-ray Raman scattering, a bulk sensitive and self-absorption free probe. Indeed, spin-orbit coupling strength and tetragonal crystal field splitting have already been experimentally determined by other authors. By focusing our attention on the O K edge and exploiting the orientation dependence of the spectra, we were able to assign features in the 528-535 eV energy loss range to specific transitions involving the Ir $5d$ orbitals. This has allowed us to extract values for the cubic crystal field splitting: 3.8 ± 0.82 eV in Sr_2IrO_4 and 3.55 ± 0.13 eV in $Sr_3Ir_2O_7$. Furthermore, we found values for the tetragonal crystal field splitting acting on the e_g states: 1.6 ± 0.82 eV in Sr_2IrO_4 and 1.9 ± 0.13 in $Sr_3Ir_2O_7$.

Abstract

This work is the first direct experimental determination of the cubic crystal field splitting in the two iridates. A complete electronic structure of the two compounds is finally achieved and the implicit theoretical assumptions, which are essential for the establishment of the $J_{\text{eff}} = 1/2$ ground state, are confirmed. Furthermore, this is one of the first X-ray Raman scattering studies at the O K edge of transition metal oxides in general: we demonstrate that this spectroscopic technique can be used to obtain a detailed picture of the electronic transitions in these materials and, more generally, our work paves the way for similar detailed studies of correlated electron systems such as the high temperature cuprate superconductors or nichelates. In particular, X-ray Raman spectroscopy is suitable for measurements in extreme environments, such as high pressure, and therefore it is a valid substitute of other techniques (*e. g.* soft X-ray absorption spectroscopy) which cannot be accomplished in such conditions.

Sommario

Tra i materiali che hanno suscitato maggiore interesse scientifico negli ultimi decenni, gli ossidi di metalli di transizione $3d$ occupano un ruolo di primo piano, in quanto caratterizzati da proprietà fisiche peculiari, come la superconduttività ad alta temperatura critica nei cuprati e la magnetoresistenza colossale nelle manganiti. Questi composti appartengono alla classe dei sistemi fortemente correlati, in cui gli elettroni della banda di valenza (derivante dagli stati $3d$ del metallo di transizione) sono descritti considerando una forte interazione elettrone-elettrone. Negli ultimi anni, l'attenzione dei ricercatori si è estesa ai metalli di transizione $4d$ e $5d$, i quali, in maniera del tutto controintuitiva, sono anch'essi soggetti ad effetti di correlazione elettronica: infatti, data la maggior estensione spaziale degli orbitali $4d$ e $5d$ rispetto agli orbitali $3d$, ci si aspetterebbe un ruolo molto ridotto della correlazione elettronica e quindi l'adozione, da parte di questi materiali, di proprietà prossime a quelle di un metallo. Al contrario, alcuni ossidi di metalli di transizione $5d$ sono isolanti, in particolare i due composti analizzati in questa tesi: Sr_2IrO_4 e $Sr_3Ir_2O_7$. Per comprendere questo comportamento inaspettato, occorre considerare l'interazione spin-orbita: infatti, se la correlazione elettronica diminuisce andando verso metalli di transizione più pesanti, l'interazione spin-orbita segue l'andamento opposto. Quando queste due interazioni diventano energeticamente comparabili, si originano nuovi fenomeni fisici, come nel caso degli iridati.

Un ulteriore stimolo nello studio degli iridati deriva dalla somiglianza tra alcune proprietà di Sr_2IrO_4 e di La_2CuO_4, il quale, se dopato, diventa superconduttore ad alta temperatura critica: i due composti hanno la medesima struttura cristallina (si veda la Figura 4.1), la cui caratteristica fondamentale è la presenza di un piano bidimensionale dove ioni di Ir (Cu) si alternano a ioni di O. La struttura elettronica è fortemente influenzata dalla presenza di questi piani, generalmente descritti considerando una la-

cuna negli stati t_{2g} (e_g) per ione di Ir (Cu). Inoltre, i due composti hanno una struttura magnetica analoga, con un ordine antiferromagnetico a lungo raggio, e gli accoppiamenti di scambio tra gli ioni di Ir sono dello stesso ordine di grandezza di quelli nei cuprati. Non sorprende, quindi, che le relazioni di dispersione nei due composti siano simili, come si osserva nella Figura 1.2. Esistono dei lavori teorici che predicono una fase superconduttiva per Sr_2IrO_4, la quale, tuttavia, non è ancora stata rivelata sperimentalmente.

Questa tesi concerne principalmente lo studio della struttura elettronica di Sr_2IrO_4 e $Sr_3Ir_2O_7$: infatti, essa è contraddistinta da uno stato fondamentale peculiare, il cosiddetto $J_{\text{eff}} = 1/2$, la cui origine può essere interpretata attraverso un modello che consideri uno ione di Ir^{4+} soggetto al campo cristallino ed all'interazione spin-orbita. Tra queste, si suppone che la maggiore perturbazione agente sui livelli $5d$ sia la componente cubica del campo cristallino: essa ne rimuove la degenerazione originando sei stati t_{2g} ad energia inferiore e quattro stati e_g ad energia maggiore. L'interazione spin-orbita agisce come ulteriore perturbazione sugli stati t_{2g} rimuovendone la degenerazione e creando un quartetto $J_{\text{eff}} = 3/2$ a minor energia e un doppietto $J_{\text{eff}} = 1/2$ a maggior energia. Nello stato fondamentale, i 5 elettroni negli orbitali $5d$ si dispongono riempiendo la banda $J_{\text{eff}} = 3/2$ e posizionando l'elettrone rimanente nella banda $J_{\text{eff}} = 1/2$, che è quindi mezza piena. Pertanto, il campo cristallino e l'interazione spin-orbita riducono la larghezza efficace della banda $5d$, riducendola a quella della sola banda $J_{\text{eff}} = 1/2$, aumentando l'effetto della correlazione elettronica. Infatti, la presenza di una repulsione coulombiana, anche debole, divide la banda $J_{\text{eff}} = 1/2$ generando una gap, come accade nel modello di Hubbard (si veda, per maggior chiarimento, la Figura 1.1): la natura isolante di questi composti è quindi spiegata a patto di considerare la forte interazione spin-orbita. Si parla, perciò, di isolanti di Mott in cui tale comportamento è indotto dallo spin-orbita. Tuttavia, le considerazioni precedenti sono valide nelle seguenti ipotesi: *i)* la separazione dei livelli generata dalla componente cubica del campo cristallino deve essere molto maggiore dell'interazione spin-orbita, così da poter trascurare gli stati e_g nel calcolo della funzione d'onda dello stato fondamentale; *ii)* la componente tetragonale del campo cristallino (sempre presente per via della non perfetta simmetria cubica del campo cristallino in materiali "reali") deve essere molto inferiore all'interazione spin-orbita, altrimenti nascerebbe un'ulteriore separazione dei livelli energetici. La seconda ipotesi è stata verificata sperimentalmente, trovando valori pari a ~ 0.01 eV per il campo cristallino tetragonale e ~ 0.4 eV per l'interazione spin-orbita; alcune misure sono state eseguite per verificare anche la prima ipotesi, ma con risultati di natura puramente qualitativa.

L'obiettivo di questa tesi è studiare la struttura elettronica di Sr_2IrO_4 e $Sr_3Ir_2O_7$ e, più specificatamente, determinare in maniera affidabile e quantitativa la componente cubica del campo cristallino. Quest'ultimo può essere misurato con varie tecniche sperimentali: ad esempio, la spettroscopia di as-

sorbimento di raggi X (XAS) alla soglia K dell'O (regime dei raggi X molli) sfrutta l'ibridazione tra gli stati $2p$ dell'O e gli stati $5d$ dell'Ir per ottenere informazioni sui livelli elettronici non occupati. La Figura 5.3 mostra alcune misure XAS, in cui però il dicroismo è molto limitato ed un'analisi che permetta di determinare valori affidabili e precisi della separazione $t_{2g} - e_g$ non è attuabile. Ciò è principalmente dovuto a due problemi intrinseci a questa tecnica: la sensibilità ristretta alla superficie del campione, dovuta alla limitazione della penetrazione dei raggi X molli ai primi piani cristallini, e l'auto-assorbimento, cioè l'assorbimento di un fotone, emesso in seguito al decadimento radiativo di un elettrone, prima che esso fuoriesca dal campione. La modifica dello spettro è resa non banale da questo processo, che dipende sia dall'energia sia dalla geometria sperimentale utilizzata. Per oltrepassare lo scoglio della sensibilità superficiale, la spettroscopia XAS può essere eseguita alle soglie $L_{2,3}$ dell'Ir: i raggi X duri hanno una maggiore lunghezza di penetrazione e garantiscono perciò un'indagine sulle proprietà del volume del materiale. Tuttavia, rimane il problema dell'auto-assorbimento. Inoltre, la lacuna di core ha un tempo di vita molto breve, che produce un aumento della larghezza di riga dei vari picchi, fino a rendere indistinguibile il contributo degli stati t_{2g} ed e_g. Si può cercare di aggirare questo ostacolo misurando gli spettri di assorbimento selezionando una particolare linea di emissione: questa tecnica permette di ottenere informazioni molto simili alla XAS con il vantaggio che, essendo il sistema decaduto ad uno stato finale meno eccitato, il tempo di vita dello stato finale è maggiore, quindi l'allargamento di riga delle transizioni di assorbimento risulta ridotto. Tuttavia la Figura 1.7 mostra che questo espediente non è sufficiente per risolvere il contributo degli stati t_{2g} ed e_g nello spettro. Altre tecniche utilizzabili sono lo scattering risonante magnetico di raggi X (RXMS) e lo scattering risonante anelastico di raggi X (RIXS) alla soglia L_3 dell'Ir: infatti, da una mappa RIXS (si veda la Figura 1.8) si nota che la maggiore intensità del segnale è situata ad energie trasferite di qualche eV: ciò è interpretato come una palese separazione tra la banda e_g vuota e la banda t_{2g} quasi piena. Tuttavia, la stima del campo cristallino cubico mediante queste tecniche (pure influenzate dall'auto-assorbimento) è molto indiretta.

In questa tesi è stata utilizzata la spettroscopia Raman a raggi X (XRS): essa consiste nello scattering anelastico di un fotone per mezzo di un elettrone di core del campione, che viene promosso in uno stato libero sopra il livello di Fermi. Gli esperimenti sono stati condotti nella beam-line ID20 del sincrotrone europeo (European Synchrotron Radiation Facility): essa è una linea di nuova costruzione, operativa dall'estate 2013, e attiva nello studio delle proprietà elettroniche e magnetiche di materiali complessi in condizioni estreme, specialmente elevata pressione. La spettroscopia XRS permette di superare sia i problemi generati dalla sensibilità superficiale, in quanto vengono utilizzati i raggi X duri, sia l'auto-assorbimento, perché le energie dei fotoni entranti ed uscenti sono distanti da qualsiasi soglia del campione.

Il principale svantaggio di questa tecnica è la sezione d'urto molto piccola, che obbliga a lunghi tempi di esposizione e conseguentemente a misure durature; inoltre, la larghezza di riga delle transizioni osservate è determinata dalla risoluzione dello strumento utilizzato e non dal tempo di vita della lacuna di core generata. Gli spettri XRS sono riportati nella Figura 5.3. La loro analisi è stata condotta sfruttando l'analogia formale tra le sezioni d'urto XRS (nel regime di dipolo) e XAS, che presentano la medesima dipendenza dal momento trasferito nella prima e dalla polarizzazione nella seconda. Ciò permette di assegnare ogni picco nella regione energetica vicino alla soglia K dell'O ad una particolare transizione di un elettrone dallo stato $1s$ ai $2p$ dell'O ibridati con gli orbitali $5d$ dell'Ir e, conseguentemente, la struttura elettronica vicino all'energia di Fermi di Sr_2IrO_4 e $Sr_3Ir_2O_7$ è completamente descritta. In particolare, siamo in grado di trovare il valore del campo cubico cristallino, che risulta essere pari a 3.8 ± 0.82 eV nel primo composto e 3.55 ± 0.13 eV nel secondo. Inoltre, è possibile calcolare la separazione tra i livelli e_g generata dal campo cristallino tetragonale: essa risulta pari a 1.6 ± 0.82 eV in Sr_2IrO_4 e 1.9 ± 0.13 eV in $Sr_3Ir_2O_7$. Essendo il campo cubico cristallino molto maggiore rispetto all'interazione spin-orbita in entrambi i composti, tutte le ipotesi necessarie alla realizzazione dello stato fondamentale $J_{\text{eff}} = 1/2$ risultano essere validate ed è possibile confermare indubbiamente che i due iridati esibiscono questo particolare stato fondamentale.

Questa tesi costituisce uno dei primi lavori sperimentali che utilizzano la spettroscopia XRS alla soglia K dell'O su ossidi di metalli di transizione: è stato dimostrato che la spettroscopia XRS permette di ottenere una raffigurazione completa della struttura elettronica vicino al livello di Fermi e può degnamente sostituire la spettroscopia XAS. L'obiettivo di questo lavoro è principalmente metodologico: è auspicabile che l'uso di questa tecnica sia ampliato ad altri ossidi di metalli di transizione (più precisamente ai più conosciuti e analizzati cuprati superconduttori ad alta temperatura critica) e soprattutto al loro studio in condizioni estreme, con particolare interesse alle alte pressioni, irrealizzabili con spettroscopia di assorbimento di raggi X molli.

Contents

List of Figures

List of Tables

CHAPTER

1

Introduction

Transition metal oxides (TMOs) with layered perovskite-like structure possess attractive properties, such as high temperature superconductivity in cuprates [1] and colossal magnetoresistance in manganites [2]. Most of these $3d$ TMOs can be classified as strongly correlated materials, for which a description in terms of non-interacting electrons fails. Electron-electron interaction is expected to become less important when moving towards heavier transition metals, because of the larger spatial extension of the $4d$ and $5d$ orbitals compared to the $3d$ ones. The absence of strong electron correlation in systems with partial filling of the valence band should lead to a metallic state for which an independent electron description is appropriate. Instead, some iridates are unexpectedly insulators. Examples are Sr_2IrO_4 [3] and $Sr_3Ir_2O_7$ [4]. This anomalous behavior has been explained by taking into account the effect of strong spin-orbit coupling of the $5d$ states [5,6]: indeed, while electron-electron correlation decreases when moving from light to heavy elements, spin-orbit coupling follows the opposite trend. At the cross-over of these two energy scales, new exotic phenomena arise and iridates offer a novel arena of intriguing properties [7–13]. In spin-orbit induced Mott insulators, as some of these iridates are named, spin-orbit coupling induces a splitting of the energy levels and a reduction of the effective bandwidth, thus enhancing the effect of electronic correlation: indeed, even a small on-site Coulomb repulsion can act to open a gap in view of the modified electronic structure [7,9] (see Figure 1.1).

Further impetus for the study of Sr_2IrO_4 comes from some affinities to the benchmark parent compound of high temperature superconductors,

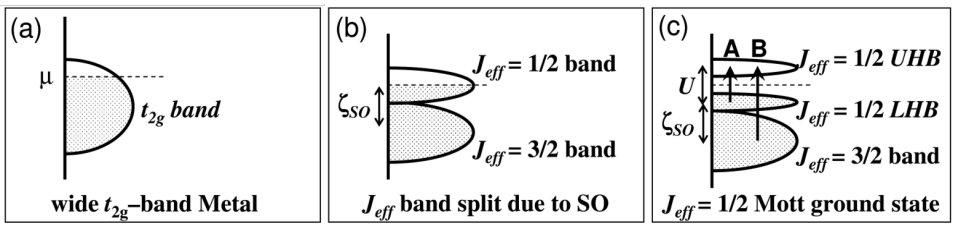

Figure 1.1: (a) t_{2g} band crossed by the Fermi level μ. (b) t_{2g} band splitting by spin-orbit coupling ζ_{SO} forming the $J_{\text{eff}} = 3/2$ and the $J_{\text{eff}} = 1/2$ bands. (c) A small Coulomb repulsion U further splits the $J_{\text{eff}} = 1/2$ band into a lower Hubbard band (LHB) and an upper Hubbard band (UHB) opening an electronic gap. [Figure taken from Ref. 7.]

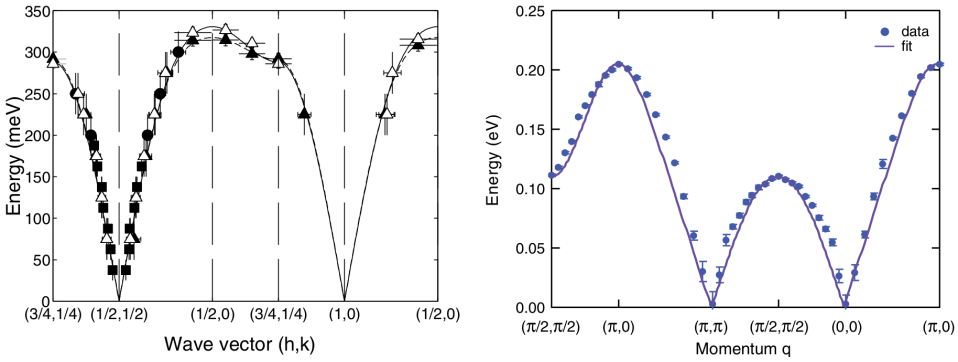

Figure 1.2: Dispersion relations of La_2CuO_4 at $T = 10$ K (left) and Sr_2IrO_4 at $T = 15$ K (right). [Figure taken from Ref. 14,15.]

La_2CuO_4: indeed, the crystal and magnetic structures of the two compounds are very similar[14–17] (see, for example, the single magnon dispersion of the two TMOs shown in Figure 1.2), as their physics is described by a single hole per Ir/Cu ion in a two-dimensional plane hosting long-range antiferromagnetic order. The connection to the cuprates is further strengthened by theoretical works predicting a possible superconducting phase in Sr_2IrO_4[11,13,15]. However, such a phase has not yet been discovered experimentally.

In the present thesis, I will mostly focus on the study of the electronic structure of Sr_2IrO_4 and $Sr_3Ir_2O_7$: the special ground state exhibited, namely the $J_{\text{eff}} = 1/2$ ground state[7,9], arises from a precise hierarchy of energies at play, in particular the crystal field splitting and the spin-orbit coupling. Within a single-ion model, the predominant perturbation to the outermost electronic states (*i. e.* Ir $5d$ orbitals) is the cubic crystal field which splits the otherwise degenerate $5d$ levels into a lower energy t_{2g} band and a higher energy e_g band. Since the cubic crystal field is usually considered much larger than the spin-orbit coupling, the five electrons occupying the $5d$ orbitals of the 4+ ionized Ir fill the t_{2g} levels in a low-spin configuration, while the e_g states are empty (Figure 1.1(a)). The second important pertur-

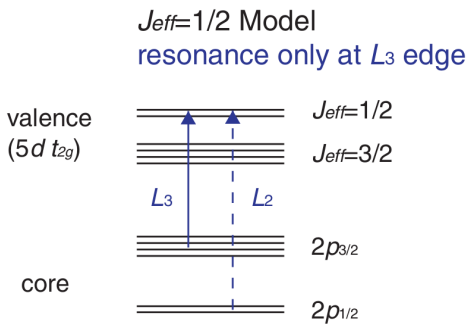

Figure 1.3: Calculations of X-ray scattering matrix elements for resonant magnetic reflection at the $L_{2,3}$ edges show an enhancement only at the L_3 edge, while no enhancement is expected at the L_2 edge. [Figure taken from Ref. 9.]

bation of the $5d$ states is the spin-orbit coupling: this acts on the t_{2g} levels splitting them in a fully occupied $J_{\text{eff}} = 3/2$ quartet at lower energy and a half occupied $J_{\text{eff}} = 1/2$ doublet at higher energy (Figure 1.1(b)). There is, however, another energy which must be carefully taken into account to properly describe the electronic structure of layered iridates: since the IrO_6 octahedra are elongated along the (001) axis of the crystal, a tetragonal contribution to the crystal field splitting alters the ideal $J_{\text{eff}} = 1/2$ state. However, the latter still remains a good description of the ground state as long as the spin-orbit coupling is dominant compared to the tetragonal crystal field splitting. Estimates in Sr_2IrO_4 [18] and other iridate compounds [19] demonstrate that the requirement of a small tetragonal crystal field compared to the spin-orbit coupling is satisfied. To identify the iridates exhibiting the $J_{\text{eff}} = 1/2$ ground state, a simple criterion has been proposed: the resonant enhancement of the magnetic reflections is expected to occur only for the L_3 edge while it is zero for the L_2 edge, as shown by X-ray scattering matrix elements calculations [9] (see Figure 1.3).

One should keep in mind, however, that the scenario of the $J_{\text{eff}} = 1/2$ ground state holds true only if the e_g states can be neglected in the description of the ground state, *i. e.* when the cubic component of the crystal field is much larger than the spin-orbit coupling, otherwise t_{2g} and e_g states would both contribute to the ground state wave function.

The aim of my work is to quantitatively determine the electronic structure near the Fermi level of the two samples with a reliable, bulk sensitive experimental technique and to verify that the conditions for the realization of the $J_{\text{eff}} = 1/2$ ground state are indeed fulfilled. Several methods can be used to estimate the cubic crystal field splitting in layered iridates, but most of them are surface sensitive probes and/or could be affected by experimental artifacts, like self-absorption. For example, X-ray absorption spectroscopy (XAS) at the oxygen K edge (soft X-ray regime) allows to probe the empty

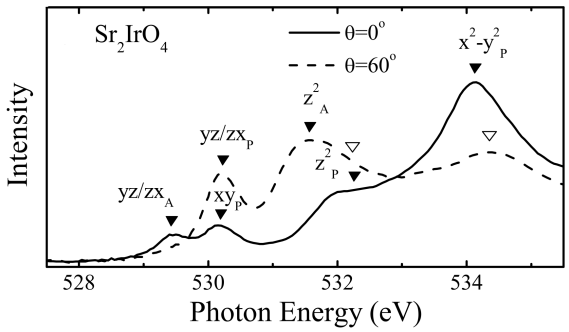

Figure 1.4: O K edge XAS spectra of Sr_2IrO_4 measured in two different experimental geometries. θ is the angle between the incident photons and the surface normal. [Figure taken from Ref. 20.]

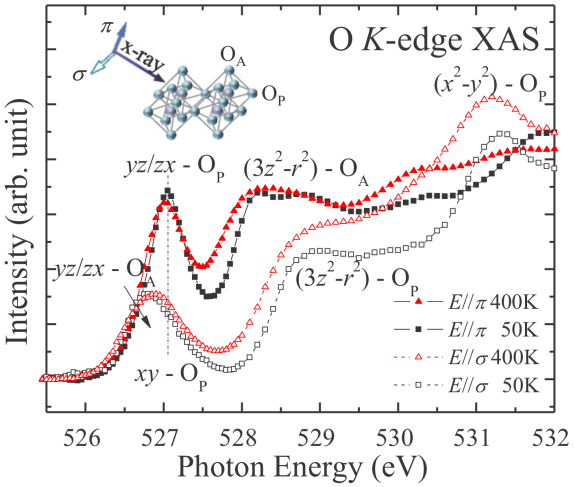

Figure 1.5: O K edge XAS spectra of $Sr_3Ir_2O_7$ taken with two perpendicular polarizations at $T = 50$ K (black) and $T = 400$ K (red lines). The experimental geometry is shown in the inset. [Figure taken from Ref. 21.]

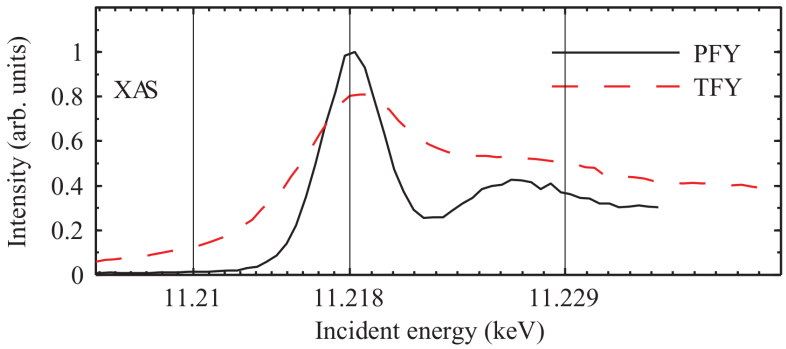

Figure 1.6: Ir L_3 edge XAS spectra of Sr_2IrO_4. Both total fluorescence yield XAS (dashed) and PFY-XAS (solid line) are reported. [Figure taken from Ref. 22.]

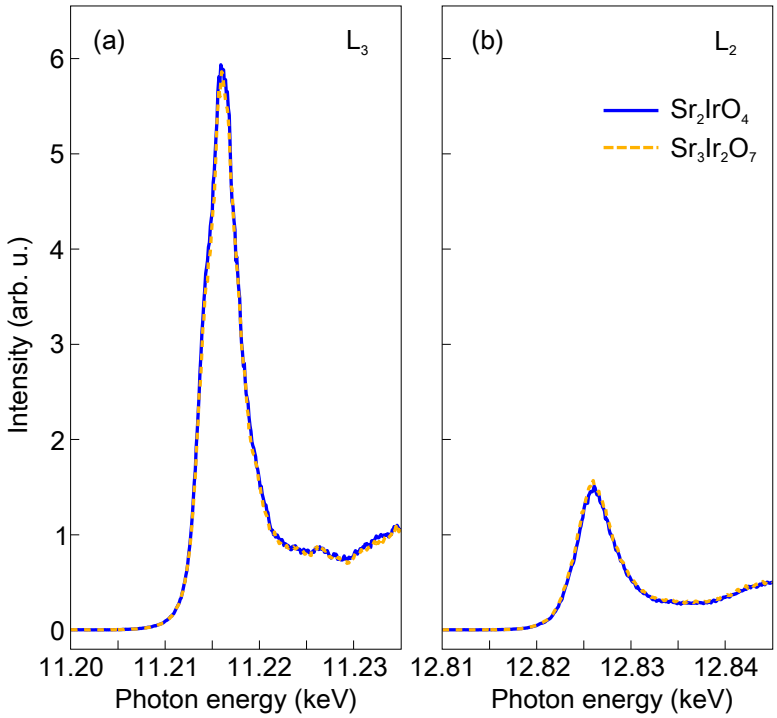

Figure 1.7: PFY-XAS spectra of Sr_2IrO_4 (blue line) and $Sr_3Ir_2O_7$ (orange dashed line) at the Ir L_3 (a) and L_2 (b) absorption edges. The selected emission lines are the Ir $L\alpha_1$ and $L\gamma_1$, respectively.

Ir $5d$ band mixed with O $2p$ orbitals (see, for example, Figure 1.4 and Figure 1.5): soft XAS provides a value for the cubic crystal field in the range 2.5 eV to 4 eV[20,21]. However, this technique suffers from self-absorption effects and it is rather surface sensitive. Self-absorption is caused by the absorption of the emitted photon (whose energy is still close to an absorption edge of the material) before it leaves the sample: this process is energy and experimental geometry dependent and modifies the spectrum in a nontrivial way. Surface sensitivity, instead, is due to the small penetration depth of soft X-rays into the sample. Since bulk and surface behavior of a material can be completely different (*e. g.* weak metallicity was found in the near-surface electronic structure of the isolating $Sr_3Ir_2O_7$[23]), surface sensitivity must be avoided. XAS at the Ir $L_{2,3}$ edges (Ir L_3 edge XAS is reported in Figure 1.6) is the next logical step: hard X-rays guarantee a larger penetration depth into the sample, but self-absorption is still a problem. Moreover, this technique suffers from the broadening of the features due to the small $2p$ core-hole lifetime ($\Gamma_{2p_{3/2}} \sim 5$ eV[24]), which washes out the details of the absorption spectrum. To circumvent this issue, XAS can be measured in partial fluorescence yield (PFY) mode: not all the photons are monitored, but only those which match a particular emission line. Therefore, the system

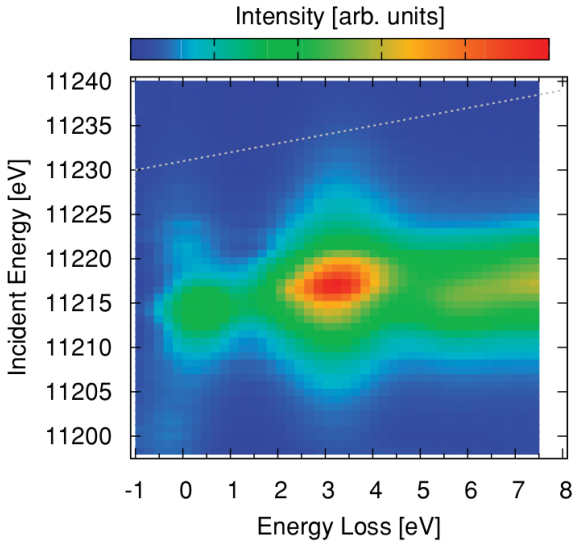

Figure 1.8: RIXS intensity map of Sr_2IrO_4 across the Ir L_3 edge: the main absorption line, due to the e_g states is ~ 3 eV away from the feature due to the t_{2g} states, located at zero energy loss. [Figure taken from Ref. 26.]

is left in a less excited state, which has a larger lifetime. The benefits of the PFY mode are undeniable, as can be seen in Figure 1.6. Figure 1.7 shows PFY-XAS at the Ir L_3 (a) and L_2 (b) edges for Sr_2IrO_4 and $Sr_3Ir_2O_7$. In these measurements, done at beam line ID20 of the European Synchrotron Radiation Facility (ESRF), $L\alpha_1$ and $L\gamma_1$ fluorescence lines were selected, corresponding to the transition of the core-hole from the Ir $2p$ to the $3d$ and $4d$ shell, respectively. Despite the advantage of this technique, it turns out that quantitative information on the cubic crystal field are still difficult to extract, because the discrimination of the features due to the t_{2g} and the e_g states is impossible. Ir L_3 edge resonant X-ray magnetic scattering (RXMS)[9,12,18,25] and resonant inelastic X-ray scattering (RIXS)[15,26–28] in the hard X-ray regime can be used as well: the fact that the intensity of both magnetic reflections in RXMS and intra-t_{2g} excitations in RIXS is maximum ~ 3 eV below the main absorption line (see Figure 1.8) is a signature of the t_{2g}–e_g splitting[29]: indeed, the main absorption line is due to the promotion of a $2p_{3/2}$ electron in the empty e_g states and the contribution of the almost full t_{2g} is marginal, while intra-t_{2g} excitations are enhanced when the $2p_{3/2}$ electron is directly promoted in the t_{2g} states. Again, however, both these techniques suffer from self-absorption, since the energy is tuned in the proximity of the $L_{2,3}$ absorption edge. Moreover, this method for the estimation of the cubic crystal field is very indirect and can be retained only at a qualitative level.

In order to overcome surface-sensitivity and self-absorption issues, we

adopt here non-resonant inelastic X-ray Raman scattering (XRS). This is a photon-in photon-out bulk sensitive probe, which is not affected by self-absorption as the energy of the incident and scattered photons are in the hard X-ray regime and far from any absorption edge of the material. The main disadvantages of this technique are the long exposure time, due to the extremely low count-rate, and the spectral broadening of the features due to the experimental energy-resolution. By exploiting the formal analogy of XAS and XRS (in the dipole limit) cross-sections, we develop a simple model for the calculation of the XRS cross-section and use it to guide the data analysis. The strong orientation dependence of the XRS signal allows us to unambiguously assign transitions to the empty Ir $5d$ states, and to extract reliable values of the crystal field parameters, such as the cubic crystal field splitting.

CHAPTER

2

X-ray Raman scattering

In the present chapter, I introduce the X-ray Raman scattering (XRS) technique. The Raman process consists of inelastic scattering of light from a sample. It was theoretically discovered and experimentally observed in the 20s[30,31]. The first experiments were performed using visible light, but soon researchers tried to replicate it using X-rays. The first unambiguous XRS spectra was reported in 1967 by Suzuki[32] for light elements such as beryllium and carbon. However, the low X-ray Raman scattering cross-section made this technique very challenging: it was only with the advent of third generation synchrotron sources that XRS became truly exploitable[33]. Nowadays, XRS is mostly used to study bulk properties of solids, liquids and systems under extreme conditions.

2.1 Introduction

Raman scattering is a photon-in photon-out process in which the photon is inelastically scattered from the sample. With this technique, different possible excitations can be studied, as shown in Figure 2.1: from phonons and magnons at low energies ($\sim 1-100$ meV), to valence electron excitations ($\sim$ 1 eV), to plasmons ($\sim$ 10 eV) and finally core electron excitations ($\sim 100-1000$ eV). In the latter case, the technique is known as X-ray Raman spectroscopy.

Core electron excitations are usually studied by means of X-ray absorption spectroscopy, in which the incident photon, whose energy is tuned close

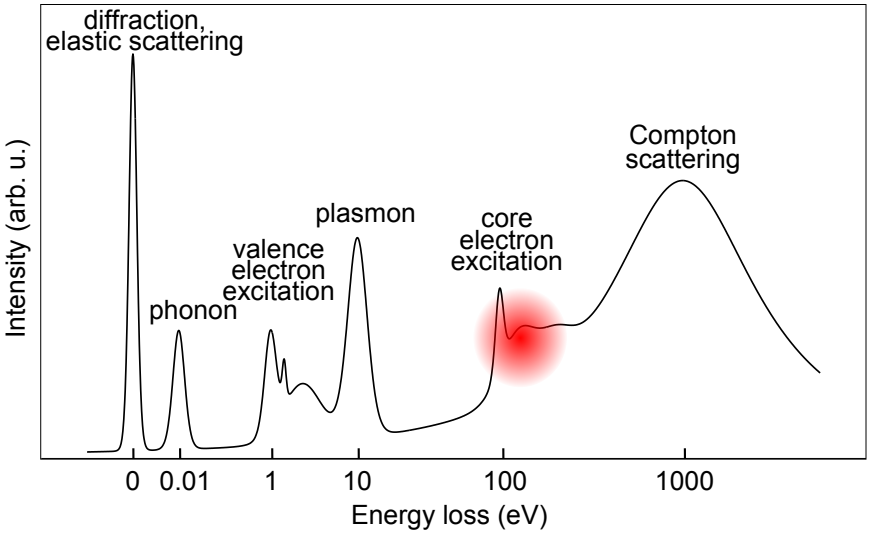

Figure 2.1: Different possible excitations depending on the energy loss: an order of magnitude is given for each feature. The energy region of our interest is highlighted in red. [Figure adapted from Ref. 34]

to an absorption edge of the material, is absorbed by an electron of the sample, which is promoted above the Fermi level. XRS offers some advantages over XAS:

- The XRS cross-section includes multipole contributions, higher than the dipolar one, depending on the magnitude of the momentum transfer $\mathbf{q}$[35]. This allows to have complementary information with respect to XAS, which instead is limited to the dipolar regime. When the magnitude of $\mathbf{q}$ is small, the XRS and XAS cross-sections become the same, if we assume that the roles of the incident energy and the polarization vector in XAS are played by the energy loss and the momentum transfer in XRS.

- XRS is a hard X-ray technique and therefore bulk sensitivity is guaranteed: at these energies typical penetration depths range from several μm (*e. g.* in iridates) to mm (*e. g.* in low Z materials, such as C). This is very important because surface effects are avoided; furthermore hard X-rays allow studies in complex sample environments, such as high pressure and high temperature. Vacuum is not required, indeed samples in the gas phase or in gaseous environment can be probed as well.

The main drawback of XRS is that it suffers from a very low count-rate and therefore requires long exposures. Moreover, the spectral broadening is often influenced by the experimental energy-resolution, which is usually comparable to the intrinsic core-hole lifetime.

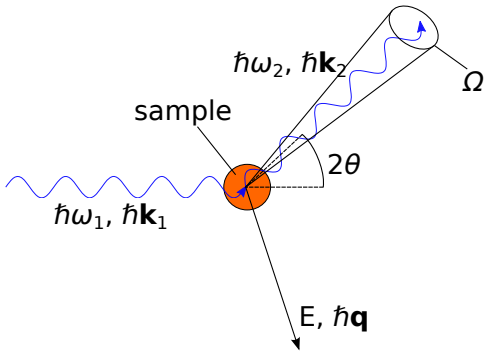

Figure 2.2: Scheme of the inelastic scattering of light by a sample: an incoming photon is scattered by the sample and loses a certain amount of its energy. The energy and momentum lost by the photon are transferred to an electron which, in the case of XRS, is a core electron.

2.2 The scattering process

The XRS process is schematically illustrated in Figure 2.2: a photon of initial energy $\hbar\omega_1$ and momentum $\hbar\mathbf{k}_1$ is inelastically scattered by an electron to a final energy $\hbar\omega_2$ and momentum $\hbar\mathbf{k}_2$ into a solid angle Ω. The energy E lost by the photon is transferred to an electron, which acquires also a momentum $\hbar\mathbf{q}$: these quantities are connected to the energy and momentum of the photon by conservation laws:

$$\hbar\omega_1 = \hbar\omega_2 + E \tag{2.1}$$

$$\hbar\mathbf{k}_1 = \hbar\mathbf{k}_2 + \hbar\mathbf{q} \tag{2.2}$$

The momentum $\hbar\mathbf{q}$ is equal in magnitude but opposite in direction to the momentum change of the photon. The magnitude q is easily calculated:

$$q = \sqrt{k_1^2 + k_2^2 - 2k_1^2k_2^2\cos(2\theta)} \tag{2.3}$$

where k_1 and k_2 are the magnitudes of $\mathbf{k_1}$ and $\mathbf{k_2}$, respectively, and 2θ is the scattering angle (*i. e.* the angle between the wave vectors).

After the scattering, the sample is left in an excited state: since, in the case of XRS, the energy loss is very high (*i. e.* in the order of $100 - 1000$ eV), a core electron is promoted to an empty state above the Fermi level. With an incident energy in the order of ~ 10 keV, the magnitude of the transferred momentum is $1 - 10$ Å^{-1}.

2.3 Theory of XRS

Following the works by Mizuno and Ohmura[36], Tohji and Udagawa[37] and more recently by Schülke[38], in this section the theory describing the XRS process is reported.

The starting point is the Hamiltonian $\mathscr{H}$ describing the interaction between the electromagnetic field, described by the vector potential $\mathbf{A}$, and the electrons of the system, treated as non-relativistic particles:

$$\mathscr{H} = \frac{1}{2m}\sum_j \left(\mathbf{p}_j + \frac{e}{c}\mathbf{A}(\mathbf{r}_j)\right)^2 + V =$$

$$= \sum_j \frac{\mathbf{p}_j^2}{2m} + V + \sum_j \left(\frac{e}{mc}\mathbf{A}(\mathbf{r}_j)\cdot\mathbf{p}_j + \frac{e^2}{2mc^2}\mathbf{A}(\mathbf{r}_j)\cdot\mathbf{A}(\mathbf{r}_j)\right) = \tag{2.4a}$$

$$= \mathscr{H}_0 + \mathscr{H}_1 + \mathscr{H}_2 \tag{2.4b}$$

where $\mathbf{r}_j$ and $\mathbf{p}_j$ are the position and momentum of the j-th electron, respectively; the summation is over all the electrons of the system. The first two terms of the Hamiltonian in Equation (2.4a) are the usual kinetic and potential operators (they describe the system in the absence of the electromagnetic field and are named $\mathscr{H}_0$ in Equation (2.4b)), while the other two terms represent the interaction radiation-matter and act as a perturbation to $\mathscr{H}_0$. The terms linear ($\mathscr{H}_1$) and quadratic ($\mathscr{H}_2$) in $\mathbf{A}$ describe the processes involving one photon (*e. g.* absorption, emission) and two photons (*e. g.* scattering), respectively. Therefore, $\mathscr{H}_2$ is the only term in which we are interested as it contributes to the XRS cross-section in first order perturbation expansion; $\mathscr{H}_1$, instead, contributes to the RIXS cross-section in second order expansion.

The transition rate for a system excited from its ground state $|g,\mathbf{k}_1\rangle$ to a final state $|f,\mathbf{k}_2\rangle$ is given by Fermi's golden rule:

$$u = \frac{2\pi}{\hbar}\left|\langle f,\mathbf{k}_2|\mathscr{H}_2|g,\mathbf{k}_1\rangle\right|^2 \delta\big((E_f+\hbar\omega_2)-(E_g+\hbar\omega_1)\big) \tag{2.5}$$

Here, $|g,\mathbf{k}_1\rangle$ and $|f,\mathbf{k}_2\rangle$ are the ground and excited states of the whole system: the initial and final electron states are $|g\rangle$ and $|f\rangle$, while the incoming and outgoing photons are in the states $|\mathbf{k}_1\rangle$ and $|\mathbf{k}_2\rangle$, respectively.

The vector potential can be expressed in terms of the photon creation and annihilation operators, $c^\dagger(\mathbf{k},\eta)$ and $c(\mathbf{k},\eta)$:

$$\mathbf{A}(\mathbf{r}) = \sum_{\mathbf{k},\eta}\sqrt{\frac{2\pi\hbar c^2}{V\omega_{\mathbf{k}}}}[\boldsymbol{\varepsilon}(\mathbf{k},\eta)c(\mathbf{k},\eta)e^{i\mathbf{k}\cdot\mathbf{r}} + \boldsymbol{\varepsilon}^*(\mathbf{k},\eta)c^\dagger(\mathbf{k},\eta)e^{-i\mathbf{k}\cdot\mathbf{r}}] \tag{2.6}$$

where η is one of the two orthogonal polarization states of the photon having wave vector $\mathbf{k}$, angular frequency $\omega_{\mathbf{k}}$ and polarization vector $\boldsymbol{\varepsilon}$; V is the volume of the system. By substituting this expression in Equation (2.5), we obtain:

$$u(f,\mathbf{q}) = \left(\frac{8\pi^3\hbar e^4}{m^2V^2\omega_1\omega_2}\right)(\boldsymbol{\varepsilon}_1\cdot\boldsymbol{\varepsilon}_2)^2\langle g|\sum_j e^{-i\mathbf{q}\cdot\mathbf{r}_j}|f\rangle\cdot$$

$$\cdot\langle f|\sum_j e^{i\mathbf{q}\cdot\mathbf{r}_j}|g\rangle\delta(E_f-E_g+\hbar\omega_2-\hbar\omega_1) \tag{2.7}$$

where the sum runs over all the electrons of the system.

Usually, in a XRS experiment, monochromatic X-rays with a definite direction and polarization are impinging onto the sample and only the photons scattered into certain solid angle $\mathrm{d}\Omega$ and within certain energy range $\mathrm{d}\hbar\omega_2$ are detected. Thus, we are interested in the probability of transition of the incoming photon in these ranges of energy and solid angle. This is obtained multiplying Equation (2.7) by the number of states which can be reached by the scattered photons in the solid angle $\mathrm{d}\Omega$ and the energy $\mathrm{d}\hbar\omega_2$ ($V\omega_2^2\mathrm{d}\Omega\mathrm{d}\hbar\omega_2/(2\pi c)^3\hbar$) and dividing by the photon flux (c/V):

$$\frac{\mathrm{d}^2\sigma}{\mathrm{d}\Omega\mathrm{d}\hbar\omega_2} = \frac{V^2\omega_2^2}{8\pi^3\hbar c^4}\sum_f u(f,\mathbf{q}) \tag{2.8}$$

The above expression is known in literature as the double differential scattering cross-section and it is often reported as:

$$\frac{\mathrm{d}^2\sigma}{\mathrm{d}\Omega\mathrm{d}\hbar\omega_2} = \left(\frac{\mathrm{d}\sigma}{\mathrm{d}\Omega}\right)_{\mathrm{Th}} S(\mathbf{q},\omega) \tag{2.9}$$

This is the ratio between the current of photons scattered into the solid angle $(\Omega, \Omega + \mathrm{d}\Omega)$ and into the energy range $(\hbar\omega_2, \hbar\omega_2 + \mathrm{d}\hbar\omega_2)$ and the current density of the incident photons times $\mathrm{d}\Omega$ times $\mathrm{d}\hbar\omega_2$. The first factor in Equation (2.9) is the Thomson scattering cross-section:

$$\left(\frac{\mathrm{d}\sigma}{\mathrm{d}\Omega}\right)_{\mathrm{Th}} = \left(\frac{e^2}{mc^2}\right)^2 \frac{\omega_2}{\omega_1}\left(\boldsymbol{\varepsilon}_1\cdot\boldsymbol{\varepsilon}_2^*\right)^2 \tag{2.10}$$

while the second factor in Equation (2.9) is the dynamic structure factor:

$$S(\mathbf{q},\omega) = \sum_f \left|\langle f|\sum_j e^{-i\mathbf{q}\cdot\mathbf{r}_j}|g\rangle\right|^2 \delta(E_f - E_g + \hbar\omega_2 - \hbar\omega_1) \tag{2.11}$$

The Thomson scattering cross-section depends only on the scattering geometry and on the energies of the incoming and outgoing photons, while the dynamic structure factor contains all the information regarding the electronic properties of the sample. It is, thus, the most important term in the cross-section and the only one we will deal with further on.

2.3.1 The dipole approximation

Now that the double differential scattering cross-section has been derived, we express it in the dipole approximation. For small momentum transfer (*i. e.* for transitions from $1s$ orbitals: $q \ll 2Z/3a_0$, where a_0 is the Bohr radius and Z is the effective atomic number), the exponential in Equation (2.11) can be expanded in series of $\mathbf{q}\cdot\mathbf{r}$:

$$e^{-i\mathbf{q}\cdot\mathbf{r}} = 1 - i\mathbf{q}\cdot\mathbf{r} + \frac{1}{2}(i\mathbf{q}\cdot\mathbf{r})^2 + \dots \tag{2.12}$$

where the second term is the dipole contribution to the scattering cross-section, the third the quadrupole contribution and so on. The first term cancels out due to the orthogonality of the eigenfunctions describing the initial and final states of the electron involved in the scattering process, while the second term dominates all the others for small $|\mathbf{q}|$.

In the dipole approximation, the dynamic structure factor $S(\mathbf{q},\omega)$ therefore reduces to:

$$S(\mathbf{q},\omega) = \sum_f \left|\langle f|\mathbf{q}\cdot\mathbf{r}|g\rangle\right|^2 \delta(E_f - E_g + \hbar\omega_2 - \hbar\omega_1) \tag{2.13}$$

This expression is formally identical to Fermi's golden rule describing the absorption process[38]:

$$T(\mathbf{q},\omega) = \sum_f \left|\langle f|\boldsymbol{\varepsilon}\cdot\mathbf{r}|g\rangle\right|^2 \delta(E_f - E_g + \hbar\omega) \tag{2.14}$$

provided that the polarization vector and the energy of the photon in XAS are substituted by the momentum transfer and the energy loss in XRS.

CHAPTER

3

Experimental setup

The experiments reported in this thesis were performed at beam line ID20 of the European Synchrotron Radiation Facility (ESRF) located in Grenoble. ID20 is one of the flagship beam lines, constructed during Phase I of the ESRF Upgrade, and operational since summer 2013. The beam line is equipped with two spectrometers for resonant and non-resonant studies of electronic and magnetic properties of solids, liquids and gases.

In this Chapter synchrotron radiation is described; then the beam line and its X-ray Raman spectrometer are introduced.

3.1 Synchrotron radiation

Synchrotron radiation occurs when charged particles moving at relativistic speed undergo a change in the trajectory of their motion, due to the interaction with a magnetic field[39]. At ESRF[40] the electrons, produced by an electron gun, are linearly accelerated to an energy of about 200 MeV before being injected in the so-called Booster synchrotron, a 300 meter-long circular accelerator in which they reach their final energy of about 6 GeV; the electrons are then sent into the storage ring, a 844 meter-long tube kept in very ultra high vacuum ($\sim 10^{-9}$ mbar), where they circle close to the speed of light and pass through different types of magnets, producing radiation.

There are two magnetic structures used to emit X-rays at ESRF: bending magnets and undulators. The former is a dipole magnet which generates

a homogeneous magnetic field, while the latter is a periodic array of dipole magnets. Electrons are guided in their circular path along the storage ring by bending magnets whose magnetic field, perpendicular to the plane of the ring, induces a Lorentz force making the path of the electrons circularly curved. In-between two bending magnets and other electron beam optics, one or more undulators are placed: the periodic magnetic field induces a sinusoidal motion of the electron beam in the horizontal plane with the same periodicity as the array of dipole magnets. The cone of the emitted radiation by an undulator is narrower than that produced by a bending magnet. Moreover, as the X-rays emitted along the undulator length interfere, only X-rays of specific wavelength constructively interfere, thus leading to the characteristic undulator spectrum with high photon fluxes at certain energies, denoted the undulator harmonics. These characteristic energies can be tuned by changing the gap between the two rows of magnets.

Undulator radiation has very peculiar properties that make it unique:

- Narrow spectral range, tuned by adjusting the gap between the two rows of magnets of the undulator and their periodicity.
- High photon flux: this gives the possibility to use techniques which otherwise suffer from low count rates.
- High brilliance: the small source size and divergence allow to obtain a spot size on the sample in the order of few μm (or even in the nm range). This is of great interest, for example, in the study of tiny amount of samples, high pressure applications and spatially resolved investigations.
- Polarization: can be set linear horizontal, to a high degree of purity.

3.2 Beam line ID20 at the ESRF

Beam line ID20 operates in the hard X-ray regime with incident photon energies ranging from 5 keV to 20 keV. It is devoted to the study of electronic and magnetic properties of solids, liquids and gases by means of resonant and non-resonant inelastic X-ray scattering. Figure 3.1 reports the scheme of the beam line.

The X-rays, produced by four undulators with a periodicity of 26 mm, diverge both in the horizontal and the vertical direction and they have a large energy bandwidth. The beam line has several optical elements in order to collect as much X-rays as possible, monochromatize them to the desired energy and focus them at the sample position.

The first optical component after the undulators is a collimating mirror (CM1): it has a cylindrical shape to vertically collimate the beam through

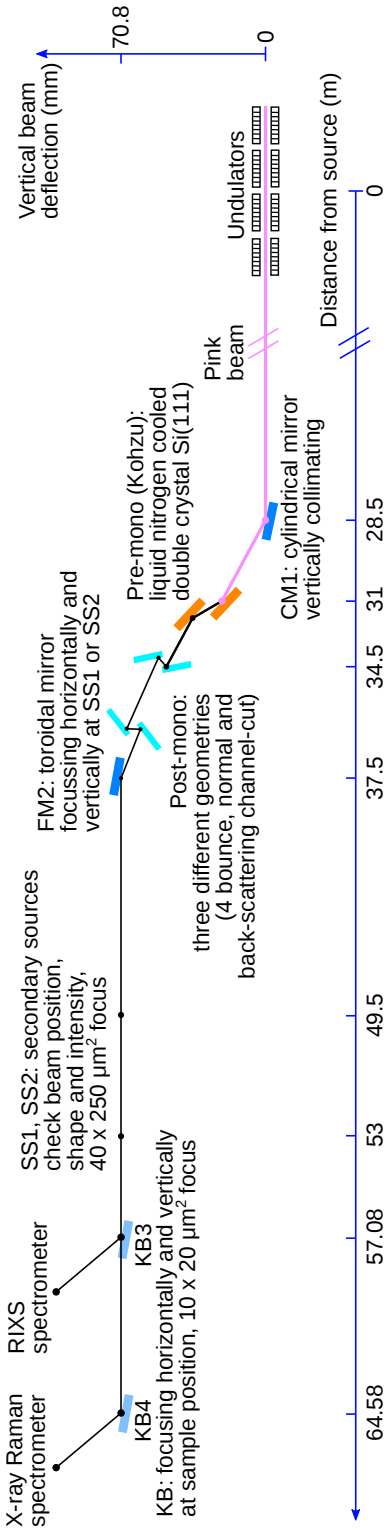

Figure 3.1: Beam line ID20 layout.

Figure 3.2: The Kohzu monochromator: the liquid nitrogen cooling system is represented in orange, the two Si crystals are reported in gray and the black arrow represents the photon beam scattered by the Si(111) surfaces.

the monochromator; the outgoing beam is still diverging in the horizontal direction.

After the collimating mirror, the beam enters a Kohzu monochromator hosting two silicon crystals (see Figure 3.2). The photons are reflected by the (111) surfaces of the two crystals according to Bragg's law [41]:

$$n\lambda = 2d\sin(\theta_{\mathrm{B}}) \tag{3.1}$$

where λ is the wavelength of the incoming photons, d is the distance between lattice planes, θ_{B} is the angle of incidence of the X-rays (*i. e.* the angle between the direction of the photons and the surface) and n is the order of diffraction. By setting the angle θ_{B}, it is possible to monochromatize the energy to the desired value: in our measurements, in which a scan of the incident energy E_i is made, the Bragg angle is adjusted to the desired value according to the following formula:

$$\theta_{\mathrm{B}} = \arcsin\left(\frac{\lambda}{2d}\right) = \arcsin\left(\frac{hc}{2dE_i}\right) \tag{3.2}$$

where h is Planck's constant, c is the velocity of light in vacuum, $a_{\mathrm{Si}} = 5.43$ Å is the lattice parameter of Si at 77 K [42], $d = a_{\mathrm{Si}}/\sqrt{h^2+k^2+l^2} = a_{\mathrm{Si}}/\sqrt{3}$ (where $h = k = l = 1$ are the Miller indices) is the lattice plane distance. According to Bragg's law, perfect crystals should have an infinitely sharp response (*i. e.* only one wavelength is reflected by the crystal); however, dynamical theory of diffraction explains the intrinsic width of a reflection. This is due to the refraction of the beam by the stack of crystal

planes and to the interference generated by the phase shift felt by the radiation while it is reflected or refracted by the crystal planes[43]. This width is called Darwin width $\Delta\theta_{\mathrm{Dw}}$, or rocking curve width, and can be expressed as:

$$\Delta\theta_{\mathrm{Dw}} = \left(\frac{\Delta E}{E}\right)\tan(\theta) \tag{3.3}$$

where $\Delta E/E$ is the energy resolution of the monochromator. In the case of the Si(111) reflection the energy resolution is $\simeq 1.35 \cdot 10^{-4}$, which corresponds to $\Delta E \simeq 1.3$ eV at an energy of ~ 10 keV.

Since the monochromator is exposed to a significant fraction of the beam power, it must be cooled by liquid nitrogen in order to prevent the heating of the crystals and the alteration of some parameters (such as the lattice constant a_{Si}), resulting in a deterioration of the beam properties (*e. g.* energy width, beam brightness and intensity). In Figure 3.2 the cooling system set-up is shown: the heat load induced by the incident X-rays is conducted through the Si crystals and transferred to the holder (represented in orange), which is liquid nitrogen cooled.

Usually, during an experiment, a better resolution is required: in the beam path, a post-monochromator can be introduced. This exploits higher order silicon reflections to achieve a resolution of the order of 0.1 eV at the energy of ~ 10 keV, at the expense of reducing the photon flux. At beam line ID20, the post-monochromator for X-ray Raman measurements is a Si(311) channel-cut crystal, providing a resolution of $\Delta E/E = 2.7 \cdot 10^{-5}$.

Then, a toroidal mirror (FM2) focuses the X-ray beam onto a point called secondary source (SS2). At this point, the spot size is 40 µm in the vertical direction and 250 µm in the horizontal one. To achieve a smaller focus on the sample, a Kirkpatrick-Baez mirror (KB) system is installed at about 0.75 m from the sample position: it is made of two elliptical mirrors with tight specifications in both slope error and surface roughness providing a focus of 10 µm × 20 µm (vertical × horizontal). The incident photon flux on the sample is in the order of 10^{13} photons/s.

3.2.1 The X-ray Raman spectrometer

The spectrometer for non-resonant inelastic X-ray scattering installed at beam line ID20 is a multiple-crystal-analyzer spectrometer (see Figure 3.3). The analyzers are kept inside six vacuum chambers (see Figure 3.4) in order to avoid scattering of the photons by air and to reduce the background noise. The chambers can separately rotate to cover a large 2θ range allowing the simultaneous measurement of different values of the momentum transfer $\mathbf{q}$.

Since the XRS cross-section is very small, the scattered photons need to be collected in a large solid angle. This can be achieved increasing the size of the analyzers, but if the crystals are flat, the X-rays will be reflected with different Bragg angles and therefore the spectral bandwidth is increased.

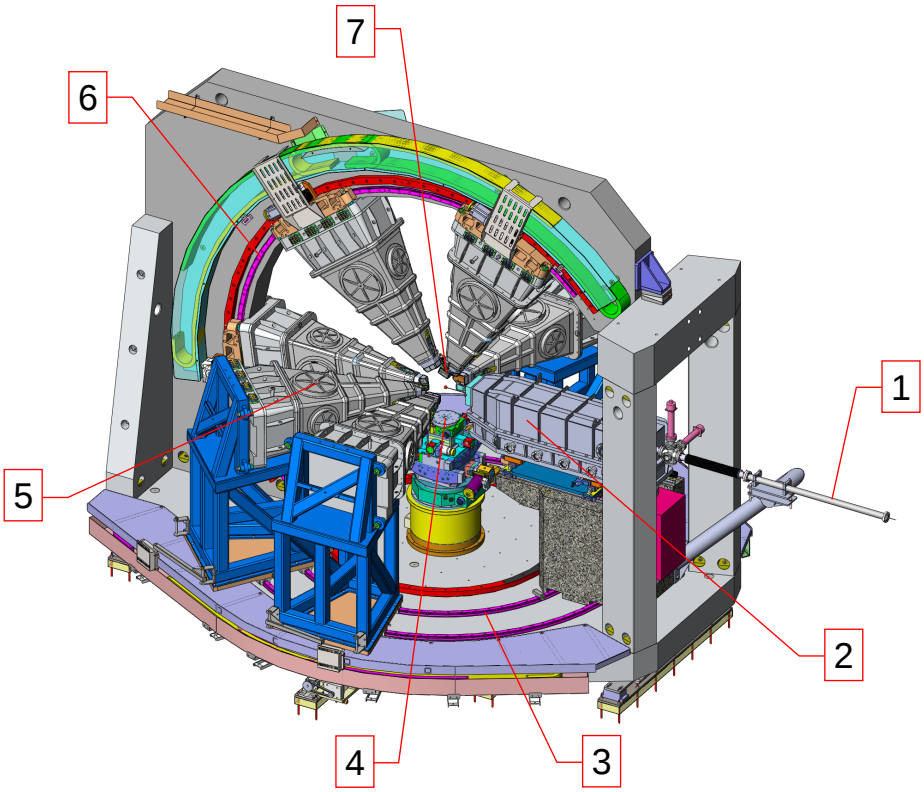

Figure 3.3: The X-ray Raman spectrometer.

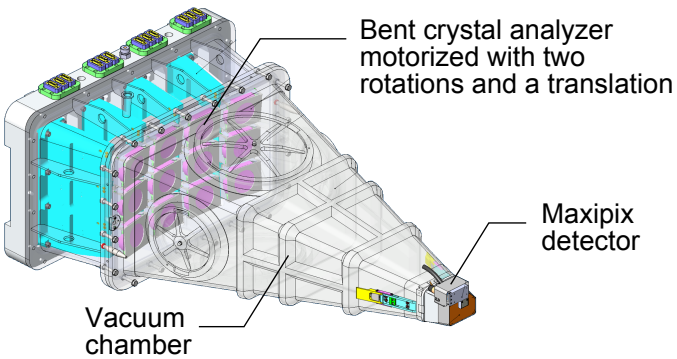

Figure 3.4: Detail of one of the six analyzer chambers of the X-ray Raman spectrometer.

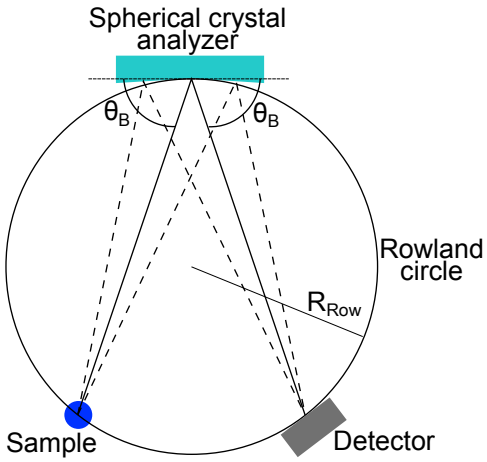

Figure 3.5: Rowland circle geometry: the photons coming from the sample are diffracted by a spherically bent crystal analyzer and focused onto the detector. Sample and detector must be placed on the Rowland circle, whose radius of curvature is half of that of the crystal.

In order to preserve a good energy resolution, but still cover a large solid angle, the crystals can be bent and the so-called Rowland circle geometry can be adopted (see Figure 3.5): sample and detector are positioned on a circle whose radius of curvature R_{Row} is equal to half the bending radius of the analyzers. In this way, X-rays scattered from the sample are focused onto the detector on the opposite side of the circle (across the line of normal incidence to the crystal surface).

The analyzers used are indeed spherically bent crystals: they are wafers of 500 µm thick Si single crystals, anodically bonded to a concave glass substrate with a curvature radius of 1 m[44]. However, due to the bending, these crystals exhibit an elastic deformation which deteriorates their properties in both energy resolution and focusing. To enhance the resolution, the analyzers are used in backscattering geometry and high reflection orders are utilized. The most commonly used configuration employs the Si(660) reflection order with a Bragg angle $\theta_{\mathrm{B}} = 88.5°$ at 9690 eV. Bent analyzers are used in those applications in which an overall resolution of ~ 0.7 eV is sufficient and a high reflected intensity is welcome. Energy scans are performed keeping the scattered energy fixed, while the incident energy is varied: this provides a constant efficiency of the spectrometer throughout the scan, because the analyzer reflectivity does not change.

The X-rays are detected by a Si hybrid pixel detector of the Maxipix family[45] (256×256 pixels of 55×55 µm^2 size). There is one Maxipix detector per analyzer chamber, therefore twelve X-ray spots are accumulated on it (see Figure 3.6) and the recorded XRS spectra can be processed either separately or by summing up data from different analyzers/chambers (see

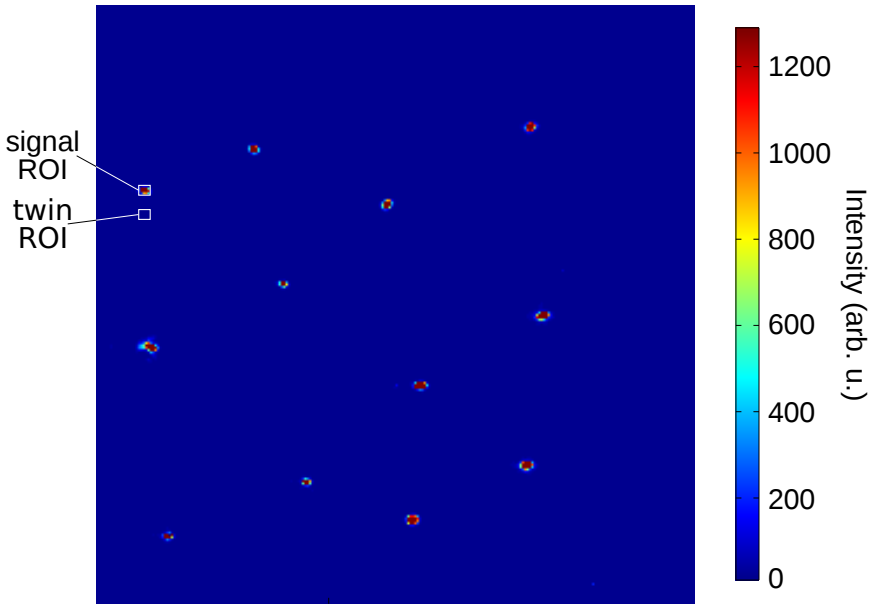

Figure 3.6: Example of an image recorded by the detector. A single chamber of the X-ray Raman spectrometer is considered. The different colors reproduce the intensity of the beam collected by the different pixels of the Maxipix detector.

as well further below).

The sample is mounted on a motorized goniometer which can be translated along the three orthogonal directions x, y and z, and rotated around these axes. This is useful to center the sample in the beam and, if the sample is a single crystal, to align it in the desired way.

3.3 Data extraction

An XRS spectrum is recorded by scanning the incident photon energy E_i at fixed steps of 0.3 eV and by collecting the photons scattered at a constant energy $E_o = 9690$ eV. Inelastic features are therefore found at energy losses of $E_i - E_o \neq 0$. At $E_i = E_o$ elastic scattering occurs, which is typically orders of magnitude stronger than the inelastic signal and can be used to calibrate the absolute energy loss and to assess the resolution of the instrument.

Energy-analyzed photons are collected on a 2D pixelated detector to physically distinguish the contributions from the different analyzers. An image as the one shown in Figure 3.6 is acquired and saved for each energy value of the spectrum. The use of pixelated detectors also allows us to select regions of interest (ROIs) around the useful signal area in order to minimize the background noise. The spectrum is obtained by integrating the signal over the ROIs for each point of the scan. Residual unwanted background

within the ROIs can be estimated, and eventually subtracted, by integrating the noise over *twin* ROIs of the same dimension and sufficiently close to the signal ROIs (see Figure 3.6).

Spectra are then normalized to a monitor value, which accounts for possible variations in the incident beam intensity, and to the counting time. Spectra associated to different ROIs can be either summed up or not depending on whether they carry the same information. In our case, we decided to sum up the contributions of the twelve analyzers of a chamber, since the corresponding momentum transfer was only slightly different. Before that, however, the different spectra are cross-correlated in order to find the best overlap between them and shifted accordingly. The chambers were positioned at different (average) scattering angles, in order to simultaneously probe different $\mathbf{q}$ values.

The error bars are calculated as the square root of the signal intensity, whose fluctuations are assumed to follow the Poisson distribution.

CHAPTER

4

Sr_2IrO_4 and $Sr_3Ir_2O_7$

The single-crystal samples studied in this work belong to the Ruddlesden-Popper series $A_{n+1}B_nX_{3n+1}$ [46] in which the alkaline earth metal A is Sr, the transition metal B is Ir and the anion X is O; n is the number of IrO_2 layers in the perovskite-like stack. Our samples are the first two compounds of this series: Sr_2IrO_4 ($n = 1$) and $Sr_3Ir_2O_7$ ($n = 2$).

In this Chapter the crystal, electronic and magnetic structures of the two samples are illustrated.

4.1 Crystal structure

Sr_2IrO_4 and $Sr_3Ir_2O_7$ are transition metal oxides with layered-perovskite structure. The single crystals were grown by R. S. Perry, E. C. Hunter, D. Prabhakaran and A. T. Boothroyd at the London Center for Nanotechnology (University College London) and the Clarendon Laboratory (University of Oxford) using the flux technique, as reported in Ref. 48.

Sr_2IrO_4 has the crystal structure of K_2NiF_4 [16] (see Figure 4.1(a)), which is very similar to that of the parent compound of high temperature superconductors, $(La,Ba)_2CuO_4$ [17]. The most important feature of the crystal is the two-dimensional IrO_2 single-layer in which the Ir ions are alternated with O ions. This plane has the same configuration as the CuO_2 layer in cuprates, which constitutes the place where the doped holes in the superconducting compounds move. Another analogy with the cuprates is the presence of coordination polyhedra: the Ir ions are surrounded by six O ions located at the

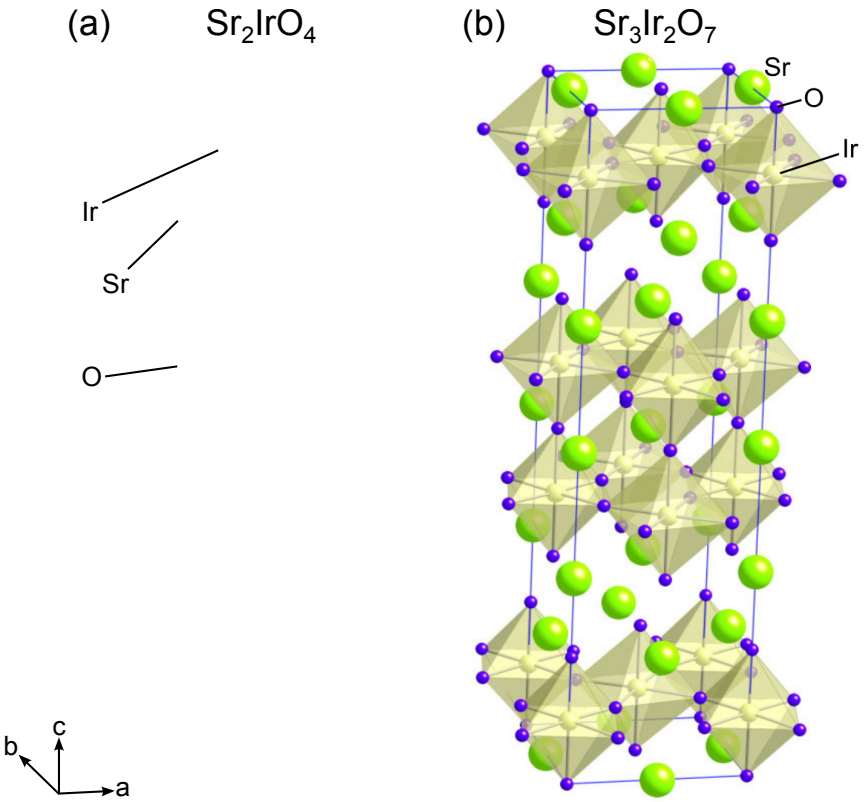

Figure 4.1: Unit cells of the two iridates (a) Sr_2IrO_4 and (b) $Sr_3Ir_2O_7$. The Ir and O ions are located at the center and at the vertices of each octahedra (shaded), respectively, while the Sr ions separate the perovskite-like stacks. [Figure adapted from Ref. 12,47.]

vertices of corner-sharing octahedra. The IrO_6 cages are rotated around the crystallographic $c = (001)$ axis by 11° and they are slightly elongated along the same axis: the distance between Ir and apical O is 4% longer than that between Ir and basal O[49]. This implies a reduction of the symmetry from cubic to tetragonal; the compound belongs to the space group $I4_1/acd$. In between the IrO_2 planes there are SrO layers.

The crystal structure of $Sr_3Ir_2O_7$ is shown in Figure 4.1(b): it is constituted by IrO_2 bi-layer stacks alternated with SrO planes. The Ir ions are surrounded by six O ions forming corner-sharing octahedra, both within a IrO_2 plane and between the planes[50]. The octahedra are elongated along the c axis by $\simeq 1.6\%$: the crystal has tetragonal symmetry and belongs to the space group $I4/mmm$. Some authors[4,51] reported more complicated structures in which the octahedra are also rotated around the c axis by 11°: within an IrO_2 plane the rotations alternate in sign, giving rise to a staggered structure, while the other plane of a bi-layer behaves in the opposite way.

4.2 Electronic structure

$5d$ TMOs have very peculiar properties, as they are characterized by a strong electron correlation. These systems can not be described by a one-electron theory, in which electrons are independently considered to move in an average potential generated by all the other electrons. The electronic and magnetic properties of these systems, in particular of $3d$ TMOs[52], have been described with some success by the Hubbard model[53]. It was mostly developed for $3d$ TMOs and can be thought as an improvement of the tight-binding model: the Hubbard Hamiltonian $\mathscr{H}_{\mathrm{Hu}}$ contains not only the kinetic term (as in the tight-binding Hamiltonian), but also a potential term arising from the Coulomb repulsion between two electrons occupying the same site. If we consider a periodic crystal with only one electron per site the Hubbard Hamiltonian is:

$$\mathscr{H}_{\mathrm{Hu}} = -t \sum_{\langle \mathbf{j},\mathbf{i}\rangle\sigma} (c^{\dagger}_{\mathbf{j}\sigma} c_{\mathbf{i}\sigma} + c^{\dagger}_{\mathbf{i}\sigma} c_{\mathbf{j}\sigma}) + U \sum_{\mathbf{j}} n_{\mathbf{j},+} n_{\mathbf{j},-} \tag{4.1}$$

where $c^{\dagger}_{\mathbf{j}\sigma}$ and $c_{\mathbf{j}\sigma}$ are the creation and annihilation operators for an electron with spin σ at lattice site $\mathbf{j}$, respectively; t and U are the energy scales of the kinetic and potential terms, respectively; $n_{\mathbf{j},+}$ and $n_{\mathbf{j},-}$ are the number of electrons with spin up or down at lattice site $\mathbf{j}$: according to Pauli's exclusion principle, they can be either 0 or 1. The first term in Equation (4.1) is the kinetic term: an electron with spin σ at lattice site $\mathbf{i}$ is annihilated and an electron with same spin is created at site $\mathbf{j}$ or vice-versa. t is the hopping integral between the two orbitals involved: since it depends on the overlap between orbitals, as a first approximation only hopping between neighboring atoms is considered (the symbol $\langle \mathbf{j}, \mathbf{i} \rangle$ means that the two sites are adjacent). According to the tight-binding model, both the hopping integral t and the bandwidth W are proportional to the overlap between orbitals, so sometimes t is replaced by W. The second term in Equation (4.1) is the potential term: the sum runs over all the lattice sites and the terms of the summation are equal to zero if the atom $\mathbf{j}$ has no electron or only one electron on it, otherwise (two electrons with different spin occupying one site) they are equal to U, which is the Coulomb repulsion felt by the two electrons.

If $U < W$ the energy cost due to the repulsion of the electrons is lower than the gain in kinetic energy and the system is metallic; when $U > W$ the strong electron repulsion forbids any hopping of the electrons and the system is insulating. Therefore, in the Hubbard model the relative magnitude of U and W determines whether a system is a metal or an insulator. $5d$ orbitals are more spatially extended than $3d$ orbitals, implying a larger bandwidth and reduced electron-electron interactions, presumably leading to a metallic state. Instead, some $5d$ TMOs are insulators: two examples are the samples under study, Sr_2IrO_4[3] and $Sr_3Ir_2O_7$[4]. The spin-orbit coupling (SOC), which is much larger in $5d$ TMOs (~ 0.4 eV[5,7]) than in $3d$

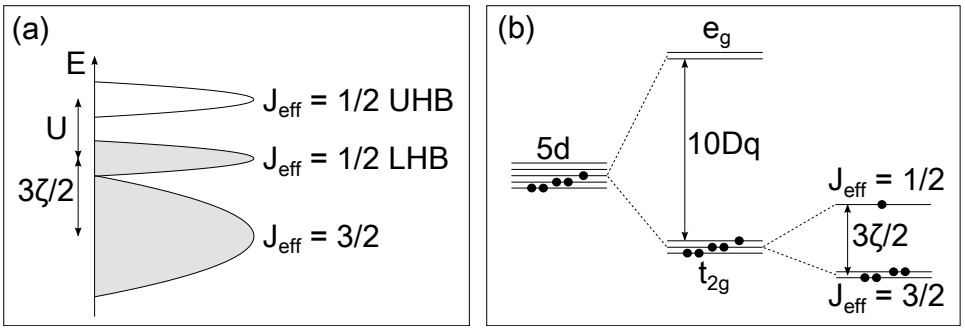

Figure 4.2: (a) t_{2g} band split by SOC ζ into a $J_{\text{eff}} = 3/2$ band and a $J_{\text{eff}} = 1/2$ band, further split by the Coulomb repulsion U into a LHB and an UHB; the bands occupied by electrons are represented in gray. (b) Schematic energy diagram for the $5d$ states split by the cubic crystal field $10Dq$ into t_{2g} and e_g states; the former are further split by SOC ζ into the $J_{\text{eff}} = 3/2$ quartet and the $J_{\text{eff}} = 1/2$ doublet. [Figure adapted from Ref. 7.]

TMOs (~ 0.02 eV[6]), was introduced to fully explain the anomalous insulating state of these systems: the SOC splits the degeneracy of the t_{2g} states, hence reducing the bandwidth and enhancing the effect of correlation. At this point, even a small Coulomb repulsion can act to open a gap between the lower Hubbard band (LHB) and the upper Hubbard band (UHB) (see Figure 4.2(a)).

The Ir atoms in Sr_2IrO_4 and $Sr_3Ir_2O_7$ are known to be 4+ ionized and arranged in a network of IrO_6 octahedra: thus the symmetry of the electrostatic field felt by the outermost electrons occupying the Ir $5d$ orbitals is not spherical, as it would be for the isolated atom, but cubic. This removes the degeneracy of the $5d$ energy levels, splitting them in six t_{2g} states at lower energy and four e_g states at higher energy. The energy difference between these levels is called cubic crystal field splitting and denoted by $10Dq$. The SOC further splits the t_{2g} states in the $J_{\text{eff}} = 3/2$ quartet at lower energy and the $J_{\text{eff}} = 1/2$ doublet at higher energy, while it does not split the e_g states (see Figure 4.2(b)). The scenario is analogous to the splitting of the p states (orbital angular momentum $L = 1$, expressed in units of $\hbar$) by SOC, but opposite in sign: one can think that the J_{eff} states are due to the addition of an *effective* orbital angular momentum $L_{\text{eff}} = -L$ to the spin angular momentum S. The 5 electrons of the Ir $5d$ orbitals full occupy the $J_{\text{eff}} = 3/2$ band and one hole is left in the $J_{\text{eff}} = 1/2$ band. This is the so-called $J_{\text{eff}} = 1/2$ ground state. The above discussion is valid only if the e_g states can be neglected in the computation of the ground state, that is if the cubic crystal field is much stronger than the SOC. The experimental validation of this hypothesis is given in Chapter 5.

In real materials, the symmetry of the crystal field is never perfectly

cubic, but it is usually lower. In the case of Sr_2IrO_4 and $Sr_3Ir_2O_7$, the elongation of the IrO_6 octahedra induces a small ($\sim$ 0.01 eV[18]) tetragonal contribution to the crystal field.

To fully understand how the t_{2g} levels are split in the presence of both SOC and tetragonal crystal field, we use a single ion model (*i. e.* only one Ir ion is considered) in which these two terms are included. The Hamiltonian is[27,28,54,55]:

$$\mathscr{H} = \zeta \mathbf{L}\cdot\mathbf{S} - \frac{\Delta}{3}L_z^2 \tag{4.2}$$

where ζ is the SOC constant and Δ is the tetragonal crystal field ($\Delta > 0$ for an octahedron elongated along the c axis). Since the e_g states do not contribute to the ground state, we limit the basis set to the t_{2g} states expressed as linear combinations of $|l, m_l\rangle$ states[56]:

$$|xy\rangle = -\frac{i}{\sqrt{2}}\big(|2,2\rangle - |2,-2\rangle\big) \tag{4.3a}$$

$$|yz\rangle = \frac{i}{\sqrt{2}}\big(|2,1\rangle + |2,-1\rangle\big) \tag{4.3b}$$

$$|zx\rangle = -\frac{1}{\sqrt{2}}\big(|2,1\rangle - |2,-1\rangle\big) \tag{4.3c}$$

The matrix elements are evaluated and the Hamiltonian diagonalized as follows. Let us separate the contribution of the SOC and the tetragonal crystal field. We suppose, for simplicity, that the magnetic moment is oriented along the $z = c$ direction. This is the case for $Sr_3Ir_2O_7$[25], while in Sr_2IrO_4 the magnetic moment lies in the basal plane[18].

- The product $\mathbf{L}\cdot\mathbf{S}$ can be expressed in terms of ladder operators, for both the orbital and the spin angular momenta, $J_\pm = J_x \pm iJ_y$, producing[57]:

  $$\mathbf{L}\cdot\mathbf{S} = L_xS_x + L_yS_y + L_zS_z = (L_+S_- + L_-S_+)/2 + L_zS_z \tag{4.4}$$

  These operators are defined such that[1]:

  $$J_\pm|j,m_j\rangle = \sqrt{j(j+1) - m_j(m_j \pm 1)}|j, m_j \pm 1\rangle \tag{4.5a}$$

  $$J_z|j,m_j\rangle = m_j|j,m_j\rangle \tag{4.5b}$$

  where the expressions above are valid for a generic angular momentum J. As an example, the matrix element $\langle xy,+|\mathbf{L}\cdot\mathbf{S}|xy,+\rangle$ is calculated

[1] All operators are expressed in units of $\hbar$.

as follows:

$$\begin{aligned}\langle xy,+|(L_+S_- + L_-S_+)/2 + L_zS_z|xy,+\rangle = \langle xy,+|L_zS_z|xy,+\rangle = \\ = \frac{1}{2}\langle xy|L_z|xy\rangle = \frac{1}{2}\frac{1}{2}\big(\langle 2,2| - \langle 2,-2|\big)L_z\big(|2,2\rangle - |2,-2\rangle\big) = \\ = \frac{1}{2}\frac{1}{2}\big(2\langle 2,2|2,2\rangle - 2\langle 2,-2|2,-2\rangle\big) = 0\end{aligned} \tag{4.6}$$

where the term containing S_+ is zero because $S_+|+\rangle = 0$ and the term containing S_- is also zero because $S_-|+\rangle = |-\rangle$ but then the integral $\langle +|-\rangle = 0$.

The full matrix for the SOC term is:

$$\underline{\mathscr{H}}^{\mathrm{SOC}} = \frac{\zeta}{2}\begin{pmatrix} 0 & 0 & 0 & 1 & 0 & -i \\ 0 & 0 & -1 & 0 & -i & 0 \\ 0 & -1 & 0 & 0 & i & 0 \\ 1 & 0 & 0 & 0 & 0 & -i \\ 0 & i & -i & 0 & 0 & 0 \\ i & 0 & 0 & i & 0 & 0 \end{pmatrix} \tag{4.7}$$

- The matrix elements for the tetragonal crystal field operator are easily calculated exploiting Equation (4.5b) if the orbitals are expressed as in Equation 4.3. For example, the matrix element $\langle xy,+|\frac{\Delta}{3}L_z^2|xy,+\rangle$ is calculated as follows:

$$\begin{aligned}\langle xy,+|\frac{\Delta}{3}L_z^2|xy,+\rangle = \frac{\Delta}{3}\langle xy|L_z\cdot L_z|xy\rangle = \\ = \frac{\Delta}{6}\big(\langle 2,2| - \langle 2,-2|\big)L_z\big(2|2,2\rangle + 2|2,-2\rangle\big) = \\ = \frac{\Delta}{6}\big(\langle 2,2| - \langle 2,-2|\big)\big(4|2,2\rangle - 4|2,-2\rangle\big) = \\ = \frac{4\Delta}{6}\big(\langle 2,2|2,2\rangle + \langle 2,-2|2,-2\rangle\big) = \frac{4\Delta}{3}\end{aligned} \tag{4.8}$$

The full matrix for the tetragonal crystal field term is:

$$\underline{\mathscr{H}}^{\Delta} = \frac{\Delta}{3}\begin{pmatrix} 4 & 0 & 0 & 0 & 0 & 0 \\ 0 & 4 & 0 & 0 & 0 & 0 \\ 0 & 0 & 1 & 0 & 0 & 0 \\ 0 & 0 & 0 & 1 & 0 & 0 \\ 0 & 0 & 0 & 0 & 1 & 0 \\ 0 & 0 & 0 & 0 & 0 & 1 \end{pmatrix} \tag{4.9}$$

Thus, a positive Δ splits the t_{2g} raising the $|xy,\pm\rangle$ orbital by a quantity equal to Δ with respect to the $|yz,\pm\rangle$ and $|zx,\pm\rangle$ orbitals.

The Hamiltonian matrix $\underline{\underline{\mathscr{H}}}$ is given by the difference of the two previous matrices. Since we are interested in the ground state of the system in the *hole* representation, the matrix must be changed in sign and becomes:

$$\underline{\underline{\mathscr{H}}} = \begin{pmatrix} \frac{4\Delta}{3} & 0 & 0 & -\frac{\zeta}{2} & 0 & \frac{i\zeta}{2} \\ 0 & \frac{4\Delta}{3} & \frac{\zeta}{2} & 0 & \frac{i\zeta}{2} & 0 \\ 0 & \frac{\zeta}{2} & \frac{\Delta}{3} & 0 & -\frac{i\zeta}{2} & 0 \\ -\frac{\zeta}{2} & 0 & 0 & \frac{\Delta}{3} & 0 & \frac{i\zeta}{2} \\ 0 & -\frac{i\zeta}{2} & \frac{i\zeta}{2} & 0 & \frac{\Delta}{3} & 0 \\ -\frac{i\zeta}{2} & 0 & 0 & -\frac{i\zeta}{2} & 0 & \frac{\Delta}{3} \end{pmatrix} \tag{4.10}$$

By diagonalizing the matrix, we can find the solution to the Schrödinger equation, *i. e.* the eigenvalues and the eigenvectors. These are the generic Kramers doublets $|0,\pm\rangle$, $|1,\pm\rangle$ and $|2,\pm\rangle$. The eigenvalues are:

$$E_{|0,+\rangle} = E_{|0,-\rangle} = -\frac{\zeta}{4}(1 - 5\delta + \sqrt{9 + 6\delta + 9\delta^2}) \tag{4.11a}$$

$$E_{|1,+\rangle} = E_{|1,-\rangle} = \frac{\zeta}{2}(1 + \delta) \tag{4.11b}$$

$$E_{|2,+\rangle} = E_{|2,-\rangle} = \frac{\zeta}{4}(-1 + 5\delta + \sqrt{9 + 6\delta + 9\delta^2}) \tag{4.11c}$$

where $\delta = 2\Delta/(3\zeta)$. They are reported as a function of Δ in Figure 4.3 for a given value of the SOC $\zeta = 0.45$ eV.

The eigenstate describing the ground state of the system is:

$$|0,-\rangle = \frac{C_0|xy,+\rangle - |yz,-\rangle - i|zx,-\rangle}{\sqrt{2 + C_0^2}} \tag{4.12}$$

where $2C_0 = 1 + 3\delta - \sqrt{9 + 6\delta + 9\delta^2}$. This is valid for a magnetic moment $\boldsymbol{\mu}$ oriented along the c axis, while if $\boldsymbol{\mu} \parallel (110)$ the ground state becomes[28]:

$$|0,-\rangle = \frac{C_0(|xy,-\rangle - i|xy,+\rangle)/\sqrt{2} + |yz,-\rangle + i|zx,+\rangle}{\sqrt{2 + C_0^2}} \tag{4.13}$$

The occupancies of the $|xy,+\rangle$, $|yz,-\rangle$ and $|zx,-\rangle$ contributing to the ground state are shown in Figure 4.4 as a function of Δ.

As it can be seen from Figure 4.3, in the limit $\Delta = 0$ the system shows a single state at lower energy and two degenerate eigenstates at higher energy (in the *hole* representation): these are the so-called $J_{\text{eff}} = 1/2$ doublet and the $J_{\text{eff}} = 3/2$ quartet, respectively. The ground state is achieved placing the single hole in the former band: this is the well-known $J_{\text{eff}} = 1/2$ ground

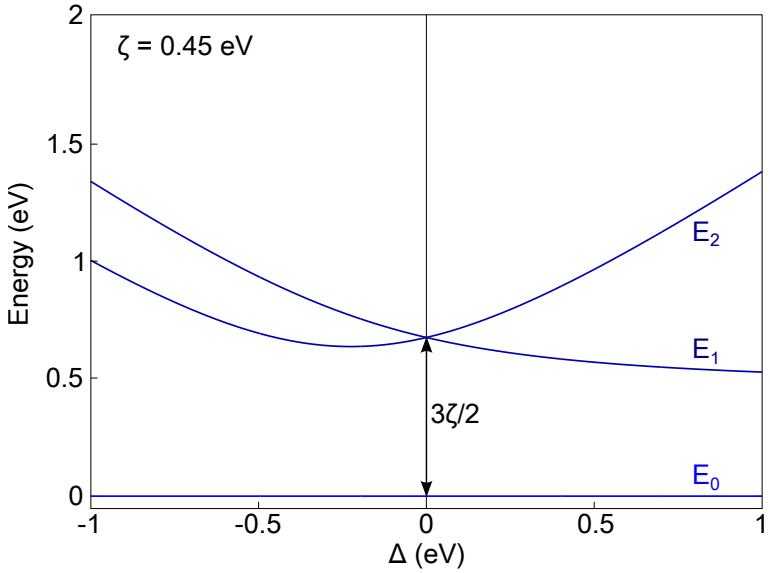

Figure 4.3: Tetragonal crystal field dependence of eigenvalues of Equation 4.11 in the *hole* representation. The ground state energy has been set to 0 and subtracted to the excited states energies. The SOC constant is set to $\zeta = 0.45$ eV.

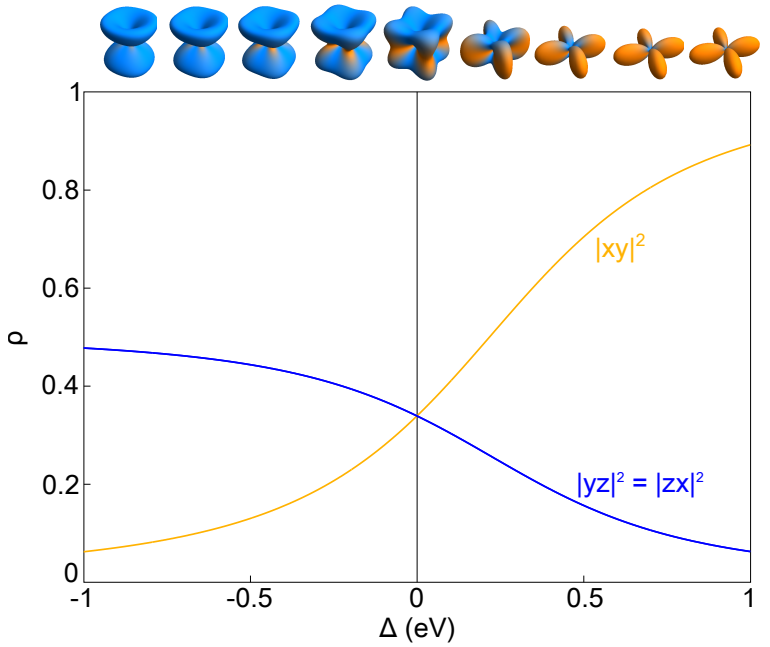

Figure 4.4: Tetragonal crystal field dependence of the ground state orbital occupancies in the *hole* representation, as derived from Equation 4.12. On the top of the Figure, an illustration of the probability density function of the ground state as combination of $|xy\rangle, |yz\rangle, |zx\rangle$ orbitals is shown as a function of Δ. [Figure adapted from Ref. 28.]

state[7,9]. Figure 4.4 shows that, for $\Delta = 0$, the ground state is composed by an even occupation of the $|xy\rangle$, $|yz\rangle$ and $|zx\rangle$ orbitals; the shape of the ground state eigenfunction is illustrated on the top of the Figure. It must be stressed that the pure $J_{\text{eff}} = 1/2$ ground state can be realized only in the limit $\Delta = 0$ which, in real materials, becomes $\Delta \ll \zeta$, *i. e.* the tetragonal crystal field must be much smaller than the SOC. In Sr_2IrO_4 and $Sr_3Ir_2O_7$ this condition is fulfilled, since $\Delta \simeq 0.01$ eV[18] and $\zeta \simeq 0.4$ eV[7]. For sizable values of Δ, instead, all the eigenstates are non-degenerate (Figure 4.3) and the generic Kramers doublets are formed.

4.3 Magnetic structure

Sr_2IrO_4 shows a weak ferromagnetism at 240 K with a saturation magnetic moment of ~ 0.1 μ_B/Ir[3,9]. The origin of this behavior is a canted antiferromagnetic structure, as reported in Figure 4.5(a): the Ir magnetic moments lie in the basal plane and are oriented along the a axis of the crystal in an antiferromagnetic way and canted by an angle of 12.2°[18]: we can assume that the magnetic moments rigidly follow the rotation of the IrO_6 octahedra.

$Sr_3Ir_2O_7$ exhibits a first magnetic transition at 285 K and a second transition at 260 K, resulting in a further increase in the magnetization; but the most striking phenomenon is the downturn in the magnetization which begins at ~ 50 K and is present only if the sample is field-cooled[4,48]. This is due to the rotation of the magnetic moments in the direction opposite to the applied field. $Sr_3Ir_2O_7$ has an antiferromagnetic structure in which the magnetic moments are oriented along the crystal c axis[25], as can be seen in Figure 4.5(b). The saturation magnetic moment is ~ 0.037 μ_B/Ir[48].

The different orientation of the magnetic moments in the two compounds is due to strong anisotropic exchange couplings between the IrO_2 layers which are present in $Sr_3Ir_2O_7$, but completely absent in Sr_2IrO_4[12]. The spin-flop transition as a function of the number of IrO_2 planes per unit cell reflects the SOC entangled nature of the $J_{\text{eff}} = 1/2$ ground state, whose wave function is spatially of three-dimensional shape (see top of Figure 4.4), in strong contrast to the cuprates with two-dimensional wave functions.

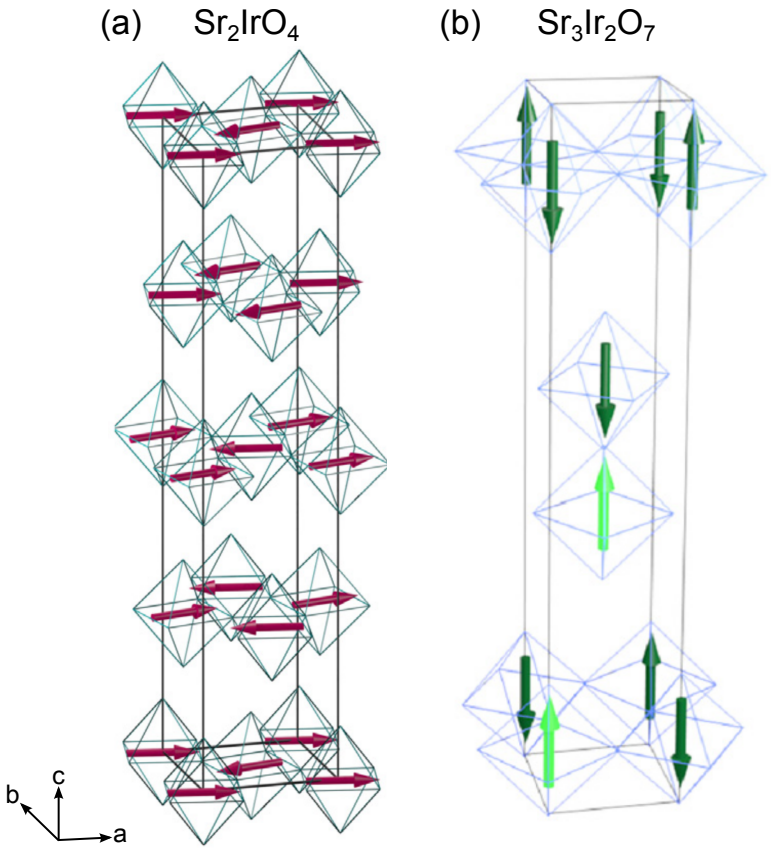

Figure 4.5: Magnetic structure of (a) Sr_2IrO_4 and (b) $Sr_3Ir_2O_7$. Sr_2IrO_4 exhibits a canted antiferromagnetic structure in which the magnetic moments lie in the basal plane and are rotated by $\sim 12°$; $Sr_3Ir_2O_7$ has an antiferromagnetic structure with moments oriented along the c axis. [Figure adapted from Ref. 18,25.]

CHAPTER

5

Results and discussion

In this Chapter the XRS spectra of Sr_2IrO_4 and $Sr_3Ir_2O_7$ are reported and analyzed. Exploiting the similarities between XRS and XAS cross-sections and with the help of a single-ion model, the cubic crystal field of the two samples is extracted.

5.1 Experimental details

During the measurements, both the Si(111) monochromator and the Si(311) post-monochromator were used to achieve an energy resolution $\Delta E_i \simeq 0.3$ eV with an incoming energy $E_i = 9690$ eV. The spot size on the sample was 10×20 μm^2. The scattered X-rays were monochromatized using Si(660) crystal analyzers in a backscattering geometry with a fixed Bragg angle of 88.5°. The resulting energy resolution was $\Delta E_o \simeq 0.7$ eV. Only one chamber of the XRS spectrometer was used and the signals from the twelve analyzers were averaged according to the procedure explained in Section 3.3. Since we wanted to obtain a spectrum comparable to a XAS measurement at the O K edge (~ 530 eV[39]), the incident energy was varied (while the outgoing energy was fixed at $E_o = 9690$ eV) in order to cover the energy loss range from 500 eV to 575 eV. The energy scan consisted of 225 points and the counting time was 30 s for each point. Several scans were acquired to improve the counting statistics.

The two scattering geometries adopted during the experiment are shown in Figure 5.1(a, b). The sample was oriented in order to have the transferred momentum $\mathbf{q}$ either along the c axis or along the a axis. The scattering angle

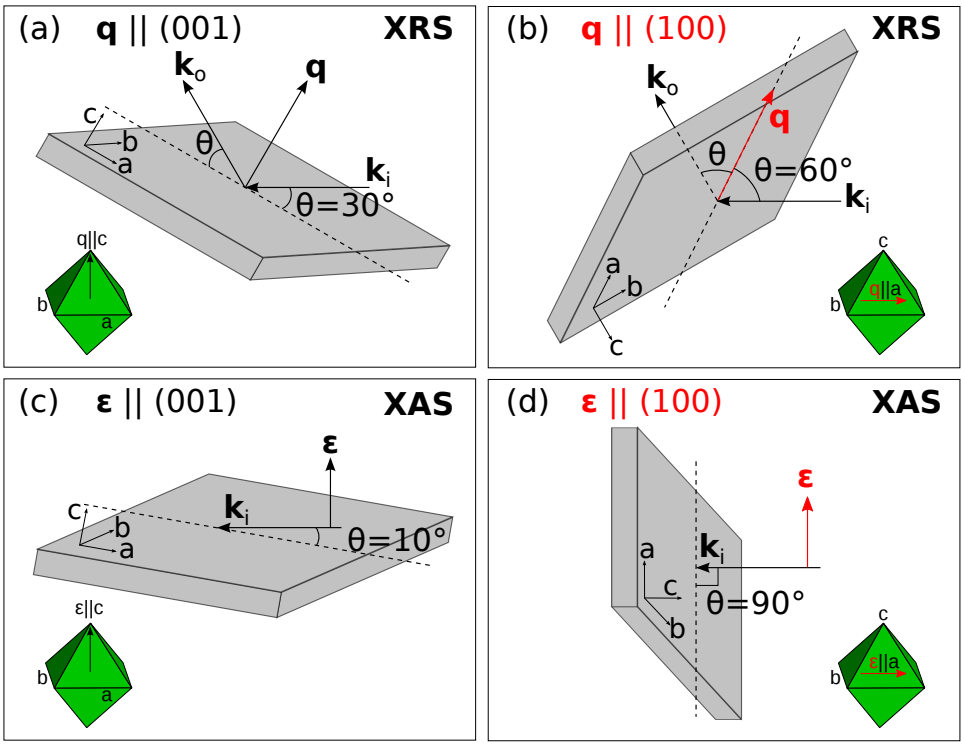

Figure 5.1: (a, b) Sketches of the two XRS scattering geometries: the sample was oriented in order to have (a) $\mathbf{q} \parallel c = (001)$ and (b) $\mathbf{q} \parallel a = (100)$; in both geometries the scattering angle was $2\theta = 60°$. (c, d) Sketches of the corresponding XAS experimental geometries: the sample was oriented in order to have (c) $\boldsymbol{\varepsilon}$ almost parallel to c and (d) $\boldsymbol{\varepsilon} \parallel a$.

2θ was in both cases 60°: according to Equation 2.3, $q \simeq 6$ Å^{-1}. This value was chosen to maximize the dipolar contribution to the scattering cross-section[58]. $Sr_3Ir_2O_7$ was measured also in a third configuration: this was similar to the geometry reported in Figure 5.1(a), but the angle of incidence on the sample was set to $\theta = 60°$ and the scattering angle was $2\theta = 120°$: this allows to keep $\mathbf{q}$ oriented along the c axis and to increase its magnitude by a factor $\sqrt{3}$ so that higher-order terms should become important in the cross-section.

Soft XAS was measured at beam line ID08 at the ESRF. The XAS experimental geometries are shown in Figure 5.1(c, d). The experiments were performed in two geometries in order to have either the polarization vector $\boldsymbol{\varepsilon}$ almost parallel to the c axis or lying in the ab plane. These two geometries perfectly match the scattering geometries chosen in the XRS measurements. XAS was measured in total fluorescence yield (TFY) mode: the incoming photon generates a deep empty state which can be filled by the radiative decay of an electron; every photon emitted is detected, irrespective of its energy.

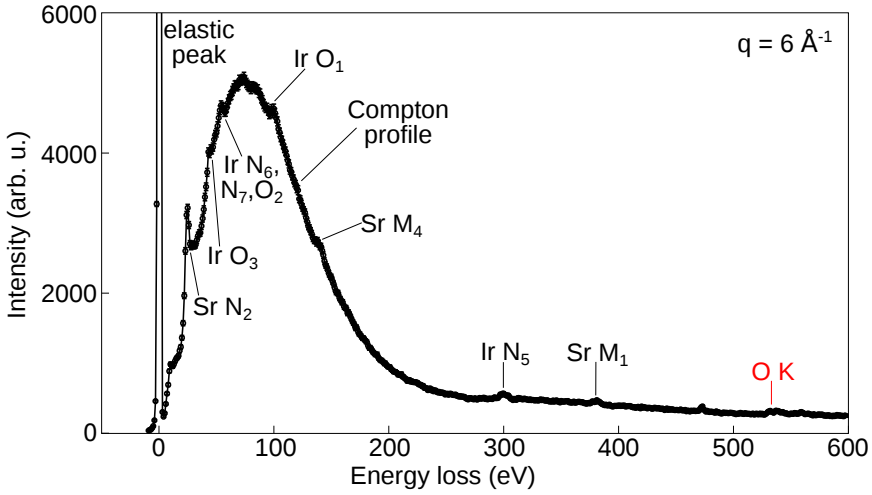

Figure 5.2: XRS spectrum of $Sr_3Ir_2O_7$ at $|\mathbf{q}| = 6$ Å^{-1} with an energy loss range $E_i - E_o$ from -10 eV to 600 eV. The elastic peak, Compton profile and different absorption edges are indicated; the O K edge is highlighted in red.

Hard XAS was performed at beam line ID20 at the ESRF with the RIXS spectrometer. Two measurements at the Ir L_3 and L_2 edges, corresponding to the transition of an electron from the $2p_{3/2}$ and the $2p_{1/2}$ states, respectively, to the continuous empty band, were done in the partial fluorescence yield (PFY) mode, in which only the photons that match a particular emission line are monitored. The fluorescence lines were the Ir $L\alpha_1$ and the Ir $L\gamma_1$, respectively, corresponding to the transition of an electron from the $3d$ to the $2p_{3/2}$ states and from the $4d$ to the $2p_{1/2}$ levels[39].

In all measurements the samples were kept at room temperature (300 K).

5.2 The XRS spectra

The XRS spectrum of $Sr_3Ir_2O_7$ is shown in Figure 5.2. As we can see, different features are present: the elastic peak at $E_i = E_o$, the Compton profile, centered at energy losses of $\sim$ 100 eV, and the various absorption edges of O, Sr and Ir. We are mostly interested in the O K edge (highlighted in red in the Figure) because the transition of the O $1s$ electron into the O $2p$ states (mixed with the Ir $5d$ band) allows the determination of the electronic structure of the sample near the Fermi energy.

The XRS spectra focused at the O K edge are shown in Figure 5.3: black (red) dots represent the $\mathbf{q} \parallel c$ ($\mathbf{q} \parallel a$) scattering geometry, in which the scattering angle was fixed to $2\theta = 60°$. Since the magnitude of $\mathbf{q}$ is small, the Compton profile is peaked around small energy losses (see Figure 5.2): in the range of our interest, its contribution is negligible and we can remove

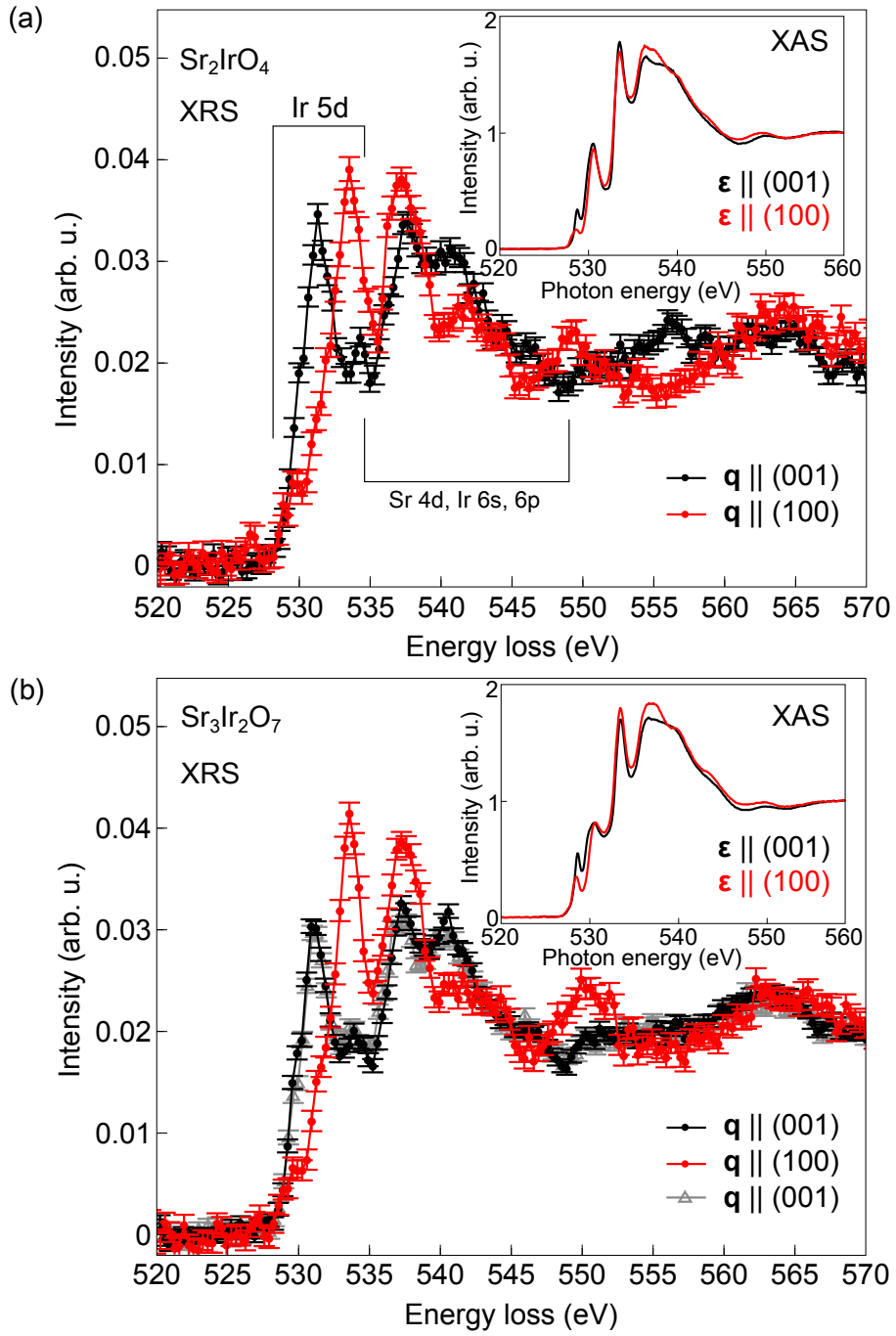

Figure 5.3: XRS spectra of (a) Sr_2IrO_4 and (b) $Sr_3Ir_2O_7$ for transferred momenta $\mathbf{q} \parallel c$ (black) and $\mathbf{q} \parallel a$ (red dots) and scattering angle $2\theta = 60°$. Gray triangles in (b) represent the XRS spectrum of $Sr_3Ir_2O_7$ with scattering angle $2\theta = 120°$. The insets show the XAS spectra at the O K edge of the two compounds for incoming polarization $\boldsymbol{\varepsilon} \parallel c$ (black) and $\boldsymbol{\varepsilon} \parallel a$ (red line).

the background by a simple linear fit of the pre-peak region at energies lower than 528 eV and then subtracting the fit to the spectrum. The spectra were then normalized to unit area.

According to XAS literature[19,20,59], the peaks in the energy loss range below $\sim$ 535 eV are associated to the promotion of an electron from the O $1s$ to the O $2p$ states, which are hybridized with the unoccupied valence states of the transition metal ion (*i. e.* Ir $5d$ band); higher energy peaks are instead associated to hybridizations with Sr $4d$ and Ir $6s$, $6p$ states. Indeed, as we have seen in Section 2.3.1, XRS spectra should be comparable to the XAS ones: the cross-section is exactly the same provided that the energy loss and the transferred momentum in XRS play the same roles as the energy of the incoming photon and the polarization vector in XAS. XAS spectra of the very same samples are also shown in the insets of Figure 5.3: continuous black (red) lines represent the $\boldsymbol{\varepsilon} \parallel c$ ($\boldsymbol{\varepsilon} \parallel a$) geometry. As we can see, the overall shape of the XAS spectra resembles that of XRS spectra, but in the latter there is a very strong dependence on $\mathbf{q}$, while the dichroism of the XAS spectra is very small and centered in the pre-peak region. This is due to surface sensitivity and self-absorption issues affecting soft X-ray absorption. The former is due to the use of soft X-rays: since their penetration depth in the sample is small, one can probe the surface of the material and not its bulk: if the surface of the sample is not perfectly crystalline or it is not clean, then the surface properties measured differ from the bulk ones. Furthermore, bulk and surface behavior of a material can be completely different: for example, weak metallicity was found in the near-surface electronic structure of isolating $Sr_3Ir_2O_7$[23]. Self-absorption effects are more subtle: the incoming photons, which have an energy very close to a resonance of the system, are absorbed by core electrons which are excited into empty states from where they radiatively decay into the initial state (elastic process) or other final states (inelastic process); the photons emitted, before leaving the sample, can be absorbed again by other electrons and consequently they are not detected. This process distorts the spectrum: the more intense absorption channels will be more affected by self-absorption with respect to the weaker channels. As a consequence, the total fluorescence yield will no longer be proportional to the XAS cross-section. These issues can be overcome by the use of XRS: this is a hard X-ray probe, allowing bulk sensitive measurements, and it does not suffer from self-absorption, since the energies of the incoming and outgoing photons are very far from any resonance of the sample.

In principle, the strong $\mathbf{q}$ dependence of the XRS spectra can be due to higher-order terms in the scattering cross-section, which are absent in the XAS cross-section. To take this into account, $Sr_3Ir_2O_7$ was measured in a geometry that allowed to increase the magnitude of the transferred momentum by a factor $\sqrt{3}$, keeping it parallel to the c axis. The spectrum is reported in Figure 5.3(b) (gray triangles): as we can see, the two spectra for $\mathbf{q} \parallel c$ look very similar, implying that quadrupole and higher-order terms

in the cross-section are negligible. Therefore, the discrepancy between XRS and XAS measurements is due to surface and/or self-absorption artifacts in the XAS spectra. On the other hand, the signal to noise ratio is much larger in XAS and the low XRS counting rate causes the acquisition of a spectrum to last several hours.

5.3 Cross-section calculation

In order to understand the spectra and to assign the features in the near-edge region (528-535 eV), we calculate the number of expected peaks and their weight by exploiting the equivalence between XRS and XAS cross-sections: this allows us to view the XRS process as the promotion of an electron from the O $1s$ orbital to the O $2p_i$ orbitals ($i = x, y, z$). Since the O is $2-$ ionized in both compounds, this transition is possible only if the O $2p$ orbitals are hybridized with the Ir $5d$ states so that an electron from the O can move to the Ir leaving a hole in the $2p$ states, which can be filled by the electron involved in the absorption process. In terms of wave function, this can be written as: $c_1|5d^5\rangle + c_2|5d^6\underline{\mathrm{L}}\rangle$, where $|c_1|^2$ and $|c_2|^2$ are the probabilities of having 5 and 6 electrons in the Ir $5d$ shell, respectively, $|5d^6\underline{\mathrm{L}}\rangle$ means that the sixth electron in the $5d$ shell comes from the ligand ion. If $c_2 = 0$, no electrons move from the ligand to the transition metal: the O $2p$ orbitals are full and the absorption process is not possible; instead, if $c_2 \neq 0$, the O $2p$ is partially empty and an O $1s$ electron can absorb a photon and be promoted to the O $2p$ orbitals. The very same process can be viewed as the movement of a hole from the Ir $5d$ to the O $2p$ states from where it is promoted to the O $1s$ orbital by the scattering process. We will treat this mechanism in the latter way.

The cross-section of the process described above can be calculated in two steps: first, we will deduce the polarization dependence of the transition O $2p_i \rightarrow 1s$, then we will calculate the hybridization strength between O $2p$ and Ir $5d$ orbitals.

5.3.1 Polarization dependence of the O $2p$ to $1s$ transitions

The starting point is the XAS cross-section (Equation (2.14)), which is analogous to the XRS one in the dipole approximation (Equation (2.13)). We have seen from the spectra in Figure 5.3 that we can safely assume the validity of this approximation.

The term containing the polarization dependence in the cross-section is: $|\langle\psi_f|\boldsymbol{\varepsilon}\cdot\mathbf{r}|\psi_i\rangle|^2$ where $\boldsymbol{\varepsilon}$ is the polarization of the incident photon, $\mathbf{r}$ is the position of the electron and ψ_i and ψ_f are the initial and final states of the electron: in our case, they are the O $2p_i$ and O $1s$ orbitals, respectively. The wave function describing the orbitals can be written in spherical coordinates

as the product between a radial function $R_n(r)$ and a spherical harmonic $Y_l^m(\theta,\varphi)$ [57]:

$$\psi_{nlm}(\mathbf{r}) = R_n(r)Y_l^m(\theta,\varphi) \tag{5.1}$$

where n, l and m are the principal, azimuthal and magnetic quantum numbers. By writing $\mathbf{r}$ in spherical coordinates as: $\mathbf{r} = r(\sin\theta\cos\varphi\hat{\mathbf{u}}_x + \sin\theta\sin\varphi\hat{\mathbf{u}}_y + \cos\theta\hat{\mathbf{u}}_z)$, where $\hat{\mathbf{u}}_x$, $\hat{\mathbf{u}}_y$ and $\hat{\mathbf{u}}_z$ are the unit vectors of the x, y, z directions, we can write the term in the cross-section as the product of a radial and an angular term:

$$\langle\psi_f(\mathbf{r})|\boldsymbol{\varepsilon}\cdot\mathbf{r}|\psi_i(\mathbf{r})\rangle = \langle R_{n_f}(r)Y_{l_f}^{m_f}(\theta,\varphi)|\boldsymbol{\varepsilon}\cdot\mathbf{r}|R_{n_i}(r)Y_{l_i}^{m_i}(\theta,\varphi)\rangle =$$
$$\langle R_{n_f}(r)|r|R_{n_i}(r)\rangle\langle Y_{l_f}^{m_f}(\theta,\varphi)|\varepsilon_x\sin\theta\cos\varphi + \varepsilon_y\sin\theta\sin\varphi + \varepsilon_z\cos\theta|Y_{l_i}^{m_i}(\theta,\varphi)\rangle \tag{5.2}$$

The radial term, depending only on the principal quantum number, is exactly the same for each $2p_i$ orbital, so we will neglect it and consider only the angular part of Equation (5.2). The initial and final states can be written in terms of spherical harmonics as [56]:

$$|1s\rangle = |0,0\rangle \tag{5.3a}$$
$$|2p_x\rangle = \frac{1}{\sqrt{2}}\big(|1,-1\rangle - |1,1\rangle\big) \tag{5.3b}$$
$$|2p_y\rangle = \frac{i}{\sqrt{2}}\big(|1,-1\rangle + |1,1\rangle\big) \tag{5.3c}$$
$$|2p_z\rangle = |1,0\rangle \tag{5.3d}$$

Now we can deduce the polarization dependence of the angular part of Equation (5.2). Let us calculate it for the $2p_x \to 1s$ transition:

$$\langle 1s|\varepsilon_x\sin\theta\cos\varphi + \varepsilon_y\sin\theta\sin\varphi + \varepsilon_z\cos\theta|2p_x\rangle =$$
$$\varepsilon_x\langle 1s|\sin\theta\cos\varphi|2p_x\rangle + \varepsilon_y\langle 1s|\sin\theta\sin\varphi|2p_x\rangle + \varepsilon_z\langle 1s|\cos\theta|2p_x\rangle =$$
$$\frac{\varepsilon_x}{\sqrt{2}}\big(\langle 0,0|\sin\theta\cos\varphi|1,-1\rangle - \langle 0,0|\sin\theta\cos\varphi|1,1\rangle\big) = \frac{1}{\sqrt{3}}\varepsilon_x \tag{5.4}$$

Thus, this transition is allowed only if the polarization has a component along the x direction. Similarly, for the $2p_y$ and $2p_z$ orbitals we obtain:

$$\langle 1s|\varepsilon_x\sin\theta\cos\varphi + \varepsilon_y\sin\theta\sin\varphi + \varepsilon_z\cos\theta|2p_y\rangle = \frac{1}{\sqrt{3}}\varepsilon_y \tag{5.5}$$
$$\langle 1s|\varepsilon_x\sin\theta\cos\varphi + \varepsilon_y\sin\theta\sin\varphi + \varepsilon_z\cos\theta|2p_z\rangle = \frac{1}{\sqrt{3}}\varepsilon_z \tag{5.6}$$

The results obtained from Equation (5.4, 5.5, 5.6) are easily interpreted if we write the operator as a linear combination of spherical harmonics:

$$\varepsilon_x\sin\theta\cos\varphi \propto \varepsilon_x\big(|1,-1\rangle - |1,1\rangle\big) \propto \varepsilon_x|2p_x\rangle \tag{5.7a}$$
$$\varepsilon_y\sin\theta\sin\varphi \propto \varepsilon_y\big(|1,-1\rangle + |1,1\rangle\big) \propto \varepsilon_y|2p_y\rangle \tag{5.7b}$$
$$\varepsilon_z\cos\theta \propto \varepsilon_z|1,0\rangle \propto \varepsilon_z|2p_z\rangle \tag{5.7c}$$

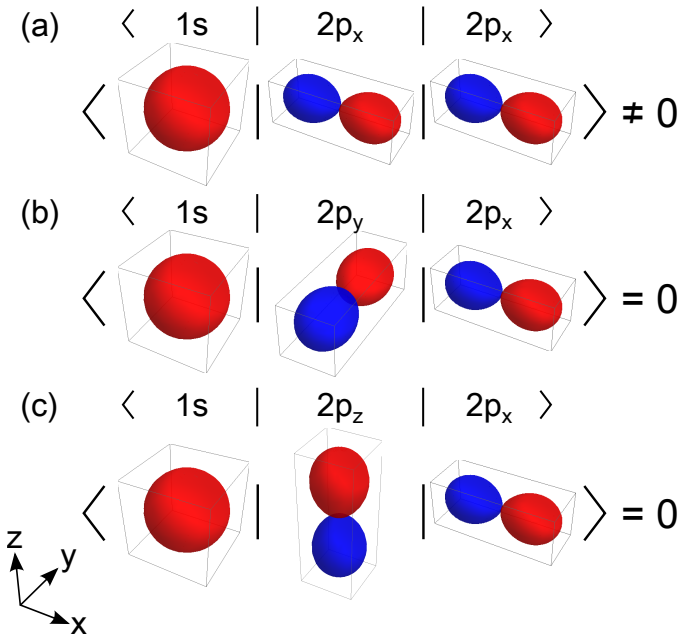

Figure 5.4: Intuitive explanation of the results obtained from Equation (5.4). The integrand in (a) is even with respect to the x, y, z directions and the integral is different from zero, while the integrands in (b) and (c) are odd and the integrals are equal to zero.

and we consider the parity of the integrand, as shown in Figure 5.4: the integrand in (a) is even with respect to the x, y, z directions, so the integral is different from zero, while the integrands in (b) and (c) are odd and the integrals are zero. As a consequence, the $2p_i \rightarrow 1s$ transition is allowed only if the incoming photon has a component of its polarization along the i direction.

The last step is to find the components of the polarization vector in the sample reference system: let θ and φ be the angles between $\boldsymbol{\varepsilon}$ ($\mathbf{q}$ in XRS) and the $z \equiv c$ and $x \equiv a$ axis, respectively, as illustrated in Figure 5.5. The three components can be written as:

$$\varepsilon_x = \sin\theta\cos\varphi \tag{5.8a}$$
$$\varepsilon_y = \sin\theta\sin\varphi \tag{5.8b}$$
$$\varepsilon_z = \cos\theta \tag{5.8c}$$

The final results of the polarization dependence of the $2p_i \rightarrow 1s$ transitions are listed in Table 5.1, where T denotes the operator of Equation (5.4, 5.5, 5.6). To obtain results consistent with the scattering geometry of the XRS measurements we must set $\theta = 0°$ for the $\mathbf{q} \parallel c$ geometry and $\theta = 90°, \varphi = 0°$ for the $\mathbf{q} \parallel a$ geometry. Thus the polarization dependences become: 0, 0, 1 and 1, 0, 0, respectively. This means that if $\mathbf{q} \parallel c$ ($\mathbf{q} \parallel a$) only

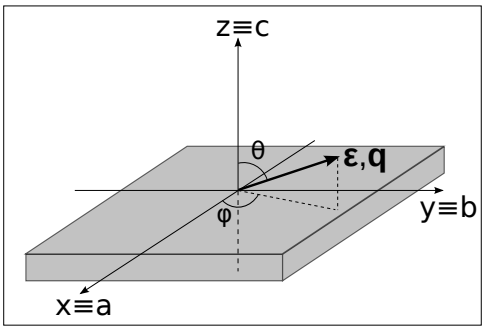

Figure 5.5: Polarization (transferred momentum) vector in the sample reference system: $\boldsymbol{\varepsilon}$ ($\mathbf{q}$) is defined by the polar and azimuth angles θ and φ.

Transition	
$\left\|\langle 1s\|T\|2p_x\rangle\right\|^2$	$\sin^2\theta\cos^2\varphi$
$\left\|\langle 1s\|T\|2p_y\rangle\right\|^2$	$\sin^2\theta\sin^2\varphi$
$\left\|\langle 1s\|T\|2p_z\rangle\right\|^2$	$\cos^2\theta$

Table 5.1: Angular dependencies of the $2p_i \rightarrow 1s$ transitions.

the transition $2p_z \rightarrow 1s$ ($2p_x \rightarrow 1s$) is permitted, while the transition of the hole from the other two $2p$ orbitals is not dipole allowed.

5.3.2 O *2p* - Ir *5d* hybridization strength

The hybridization between Ir and O orbitals allows a hole to move from the Ir half-filled $5d$ band to the O empty $2p$ band. The hybridization strength is calculated according to the orbital overlap model, as explained by Slater and Koster[60]: the hopping integral $t_{pd\mu}$ between p and d orbitals can be written as:

$$t_{pd\mu} = V_{pd\mu} r^{-\alpha} \tag{5.9}$$

where $V_{pd\mu}$ is a constant depending on the bond type ($\mu = \sigma$ for a σ-bond and $\mu = \pi$ for a π-bond), r is the distance between the two atoms and $\alpha = 7/2$[61]. The constants $V_{pd\pi}$ and $V_{pd\sigma}$ are related by $V_{pd\sigma} = -\sqrt{3}V_{pd\pi}$ according to Muffin-Tin orbital theory[61,62].

Since the hopping integral is inversely proportional to the distance between the atoms involved and the octahedra are distorted along the c axis, we should separate the contribution of apical (A) and in-plane (P) oxygens. Let us consider the apical O first: p_x and p_y hybridize with zx and yz, respectively, while p_z mixes with $3z^2 - r^2$; in the case of in-plane O, instead, $2p_x$ and $2p_y$ hybridize with xy, $3z^2 - r^2$ and $x^2 - y^2$, while $2p_z$ is mixed with

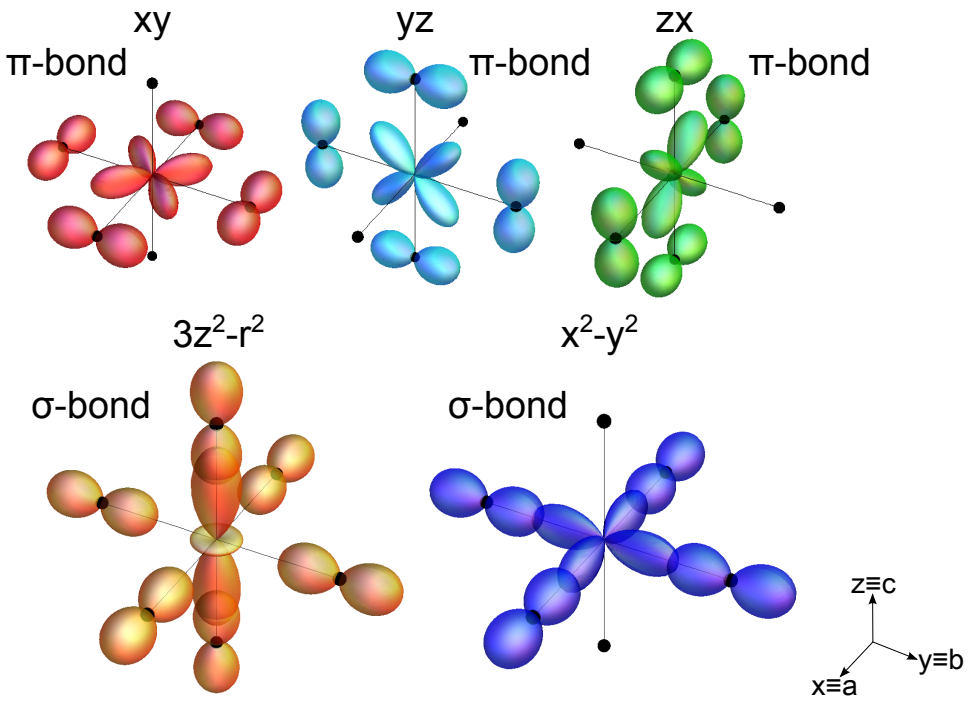

Figure 5.6: Sketch of the O $2p$ orbitals participating in the hybridization with the Ir $5d$ orbitals.

yz and zx. The bond between the t_{2g} and the $2p$ orbitals is a π bond, while a σ bond links e_g with $2p$ orbitals. This is summarized in Figure 5.6.

5.3.3 Results of the cross-section calculation

By merging the results obtained from the polarization dependence of the O $2p_i \rightarrow 1s$ transitions and the hybridization strength calculation of the O $2p$ - Ir $5d$ orbital mixing, we obtain the final cross-sections, which are listed in Table 5.2 for the two scattering geometries used in the measurements and for the different possible hybridizations. In view of the small tetragonal crystal field of the two compounds, we assume that the t_{2g} states are split by SOC only. Thus, the xy, yz, zx orbitals are equally occupied ($n_{xy} = n_{yz} = n_{zx} = 1/3$, Equation (4.12)) and the e_g states are filled by four holes ($n_{3z^2-r^2} = n_{x^2-y^2} = 2$). Note that the hopping integral is squared, because the probability of mixing between orbitals goes as t^2, and that the number of O in the IrO_6 is taken into account.

As can be seen from Table 5.2, when $\mathbf{q} \parallel a$, four transitions are allowed, due to the hopping of a hole from the Ir zx to the $2p_x$ of apical O and the hopping from xy, $3z^2 - r^2$ and $x^2 - y^2$ to the $2p_x$ of in-plane O; the hole is then promoted from the $2p_x$ to the $1s$ orbital by absorbing a photon. Instead, when $\mathbf{q} \parallel c$, the hole can move from the yz or zx to the $2p_z$ orbital

	$\mathbf{q} \parallel a$	$\mathbf{q} \parallel c$
$xy/yz/zx_A$	$2V_{pd\pi}^2 n_{zx} r_A^{-2\alpha}$	
$xy/yz/zx_P$	$2V_{pd\pi}^2 n_{xy} r_P^{-2\alpha}$	$4V_{pd\pi}^2 n_{zx} r_P^{-2\alpha}$
$3z^2 - r_A^2$		$2V_{pd\sigma}^2 n_{3z^2-r^2} r_A^{-2\alpha}$
$3z^2 - r_P^2$	$V_{pd\sigma}^2 n_{3z^2-r^2} r_P^{-2\alpha}$	
$x^2 - y_A^2$		
$x^2 - y_P^2$	$\sqrt{3} V_{pd\sigma}^2 n_{x^2-y^2} r_P^{-2\alpha}$	

Table 5.2: Results of the cross-section calculation.

of in-plane O and from $3z^2 - r^2$ to the $2p_z$ of apical O; the hole can then be scattered from the $2p_z$ to the $1s$ orbital.

5.4 Constrained fit of the spectra

The fit of the spectra was made using a Pearson type VII distribution for each feature in the energy range of interest:

$$p(\mathbf{P}, x) = \frac{A}{\left(1 + \left(2^{\frac{1}{\mu}} - 1\right)\left(2\frac{x - x_0}{w}\right)^2\right)^{\mu}} \tag{5.10}$$

where A is the amplitude of the curve; x_0 is the peak center; w is the full width at half maximum (FWHM); μ is a parameter which modifies the shape of the curve: if $\mu = 1$ the curve is Lorentzian while if $\mu \to \infty$ the curve is Gaussian; $\mathbf{P}$ is the vector whose elements are the fit parameters A, μ, w and x_0.

According to the results obtained from the cross-section calculation, four peaks are expected for $\mathbf{q} \parallel a$ and only two peaks when $\mathbf{q} \parallel c$. Therefore, we conformed the number of fitting curves to these results: in the $\mathbf{q} \parallel a$ ($\mathbf{q} \parallel c$) geometry, four (two) curves are used to represent the experimental data and one (two) curve to account for the higher energy features. The relative spectral weights of the curves are proportional to the calculated ones (Table 5.2). The constrained fits are shown in Figure 5.7(a, b) for Sr_2IrO_4 and in Figure 5.7(c, d) for $Sr_3Ir_2O_7$: the open circles represent the experimental data, the fit is reported as thick solid lines, while the single features are plotted as thin solid lines.

It must be stressed that the only free parameters in the fit are the energy positions and FWHM of the features, while the spectral weights are fixed to the calculated values (apart from a common scaling factor to better adjust all the amplitudes to the experimental data). Table 5.3 reports the energy positions and the FWHM of the peaks, as resulting from the fit. As we

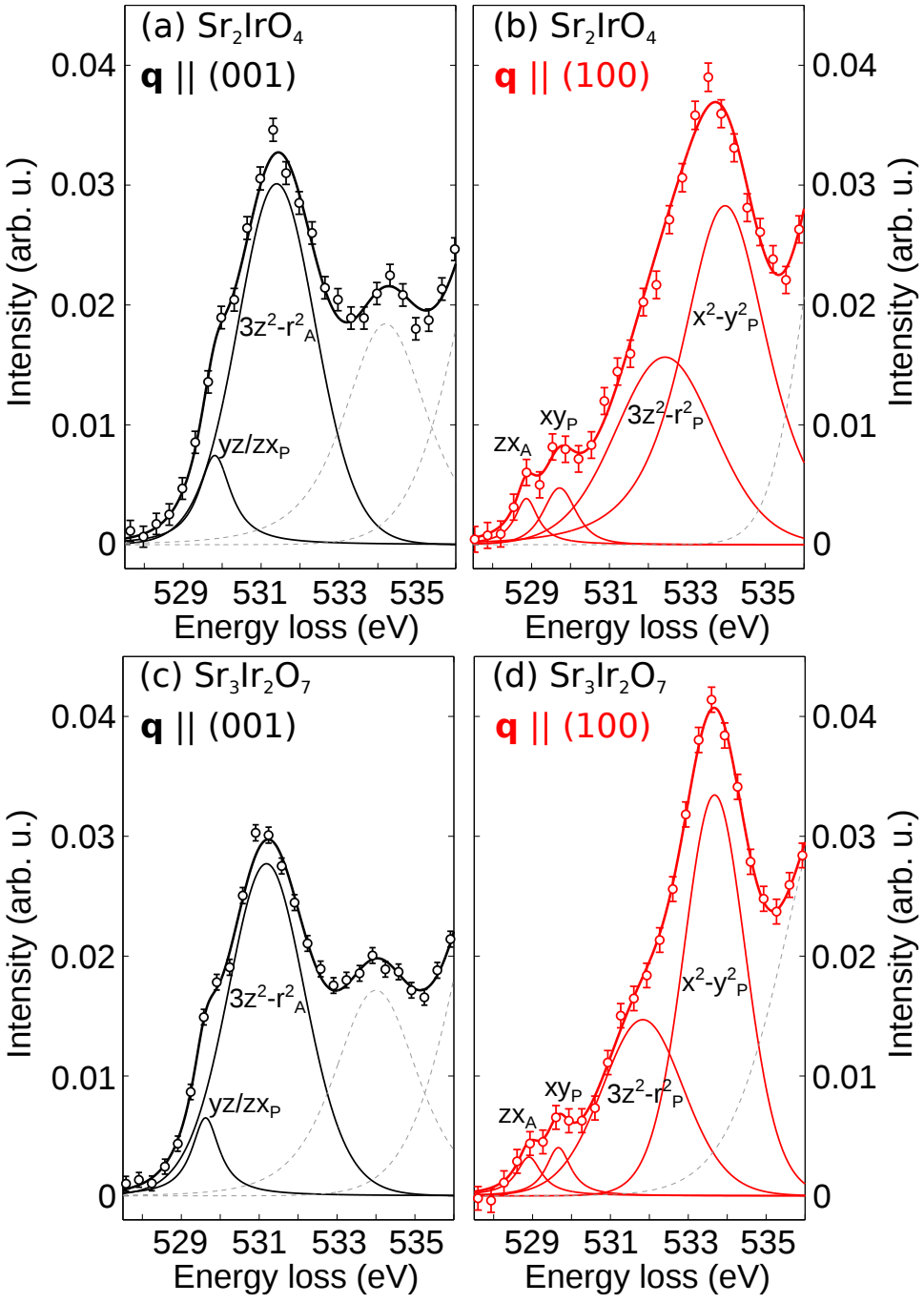

Figure 5.7: Constrained fit of the XRS spectra of (a, b) Sr_2IrO_4 and (c, d) $Sr_3Ir_2O_7$ in the two scattering geometries: (a, c) $\mathbf{q} \parallel c$ and (b, d) $\mathbf{q} \parallel a$. Experimental data are reported as open circles, the thick solid lines are the fitting curves, the single features and the extra peaks resulting from the fit are plotted as thin solid and dashed lines, respectively.

	Energy loss (eV) Sr_2IrO_4	FWHM (ev) Sr_2IrO_4	Energy loss (eV) $Sr_3Ir_2O_7$	FWHM (eV) $Sr_3Ir_2O_7$
$xy/yz/zx_A$	528.9 ± 0.11	0.71 ± 0.35	528.9 ± 0.10	0.78 ± 0.30
$xy/yz/zx_P$	529.8 ± 0.05	1.0 ± 0.17	529.6 ± 0.03	0.87 ± 0.10
$3z^2 - r^2_A$	531.4 ± 0.05	2.4 ± 0.18	531.2 ± 0.05	2.4 ± 0.15
$3z^2 - r^2_P$	532.4 ± 0.75	3.0 ± 0.67	531.8 ± 0.12	2.5 ± 0.26
$x^2 - y^2_A$				
$x^2 - y^2_P$	534.0 ± 0.35	2.6 ± 0.46	533.7 ± 0.05	1.9 ± 0.06

Table 5.3: Energy position and FWHM of the absorption features resulting from the fit of the XRS spectra of Sr_2IrO_4 and $Sr_3Ir_2O_7$ [1].

can see from Figure 5.7, the agreement between the experimental data and the simulations is remarkable in both scattering geometries and for both samples: this allows us to assign each feature to the corresponding transition of a hole from a particular Ir $5d$ state to a specific O $2p$ orbital. The labels of each peak of Figure 5.7 denote the particular transitions: for example, the intense features at 531.4 (531.2) and 534.0 (533.7) eV for Sr_2IrO_4 ($Sr_3Ir_2O_7$) correspond to the transition of a hole from the Ir $3z^2 - r^2$ state to the $2p_z$ orbital of an apical O and from the Ir $x^2 - y^2$ state to the $2p_x$ orbital of an in-plane O, respectively.

The peak assignment is consistent with the work of Moon *et al.*[20] on Sr_2IrO_4, Schmidt *et al.*[63] on Sr_2RuO_4 and Park *et al.*[21] on $Sr_3Ir_2O_7$.

5.5 Extraction of the cubic crystal field

From the results obtained in the previous section, we can extract the cubic crystal field of the two compounds. This is calculated as the energy difference between the centers of mass of the t_{2g} and the e_g states, taking into account those peaks due to transitions to apical or in-plane O only. Since the tetragonal crystal field in the two compounds is very small ($|\Delta| \sim 0.01$ eV[18]), the t_{2g} states are supposed to be split only by SOC. Taking this into account and considering that for $\Delta \sim 0$ the splitting between the t_{2g} is $\sim 3\zeta/2$ (Equation (4.11)), we obtain a value of the cubic crystal field of $10Dq = 3.8 \pm 0.82$ eV in Sr_2IrO_4 and 3.55 ± 0.13 eV in $Sr_3Ir_2O_7$,

[1] The confidence intervals of the fitting parameter are calculated as the square root of the diagonal elements of the covariance matrix, given by the following expression:

$$\mathrm{cov}(\mathbf{P}) = \frac{1}{N-k} \sum_{i=1}^{N} \left(y_i - p(\mathbf{P}, x_i)\right)^2 \left(\underline{J_p}^T \underline{J_p}\right)^{-1} \tag{5.11}$$

where N and k are the number of data points (x_i, y_i) to the fit and the number of fitting parameters (*i. e.* the size of $\mathbf{P}$), respectively; $\underline{J_p}$ is the Jacobian matrix[64].

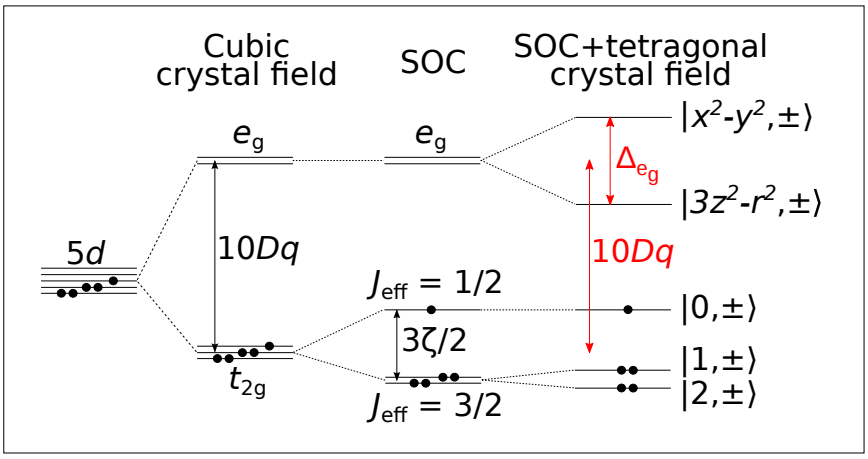

Figure 5.8: From left to right: Ir $5d$ levels are degenerate if no crystal field or SOC is considered; the cubic component of the crystal field splits this band into the t_{2g} and the e_g levels; SOC further splits the t_{2g} states into a $J_{\text{eff}} = 3/2$ and a $J_{\text{eff}} = 1/2$ band; the tetragonal component of the crystal field mixes these bands forming the Kramers doublets $|0,\pm\rangle$, $|1,\pm\rangle$ and $|2,\pm\rangle$. The values we measured are highlighted in red.

	$10Dq$ (eV)	ζ (eV) [7]	$\Delta(t_{2g})$ (eV) [18]	$\Delta(e_g)$ (eV)
Sr_2IrO_4	3.8 ± 0.82 eV	~ 0.4	~ 0.01	1.6 ± 0.82
$Sr_3Ir_2O_7$	3.55 ± 0.13 eV	~ 0.4	~ 0.01	1.9 ± 0.13

Table 5.4: Values of the cubic crystal field splitting, SOC and tetragonal crystal field splitting for Sr_2IrO_4 and $Sr_3Ir_2O_7$.

considering $\zeta = 0.4$ eV [7]. A schematic energy diagram showing the t_{2g} and e_g levels split by the crystal field and SOC is reported in Figure 5.8. The result is consistent with estimates of $10Dq$ extracted from XAS [20,21] and RXMS/RIXS [55] measurements.

The cubic crystal field is very large when compared to the other energies at play: spin-orbit coupling and tetragonal crystal field (see Table 5.4 for a summary of the Ir $5d$ band splitting by crystal field and SOC), therefore validating the hypothesis that $10Dq$ is the dominant energy scale and that the e_g states do not participate to the ground state of the system, which is fully determined by a linear combination of the t_{2g} states, as stated by Equation (4.12, 4.13).

Furthermore, from the constrained fit, we are able to deduce the energy separation between the e_g states: since these levels are not split by SOC, the only energy acting on them is the tetragonal crystal field (see Figure 5.8). We obtain 1.6 ± 0.82 eV in Sr_2IrO_4 and 1.9 ± 0.13 eV in $Sr_3Ir_2O_7$. Note that the $x^2 - y^2$ orbital is higher in energy than the $3z^2 - r^2$: thus we expect

a minor role of the electronic repulsion in the latter orbital, leading to an elongation of the IrO_6 octahedra along the c axis. This is consistent with X-ray diffraction structural studies of the two compounds[3,50]. The fact that the tetragonal crystal field acting on the e_g states is very large is in agreement with the requirement of a small Δ: indeed, the description of the tetragonal crystal field acting on the $5d$ states requires two parameters, Ds and Dt. The splitting of the t_{2g} and the e_g states is then given by $3Ds-5Dt$ $(=\Delta)$ and $4Ds+5Dt$, respectively[65]. A small Δ implies $3Ds \simeq 5Dt$ and thus a finite splitting of the e_g states is compatible with the realization of the $J_{\text{eff}} = 1/2$ ground state in the two iridates.

CHAPTER

6

Conclusions

The present thesis dealt with the study of Sr_2IrO_4 and $Sr_3Ir_2O_7$, two perovskite-like $5d$ transition metal oxides whose peculiar electronic structure has recently attracted much attention. The singular ground state exhibited, the so-called $J_{\text{eff}} = 1/2$ ground state, is due to a particular hierarchy of energies at play: cubic crystal field $10Dq$, due to the octahedral charge density felt by the outermost Ir $5d$ electrons, spin-orbit coupling ζ, which is large in $5d$ compounds, and the tetragonal component Δ of the crystal field, due to a slight elongation of the IrO_6 cage. In the specific iridates studied in this work, $10Dq$ is thought to be the largest energy and causes the splitting of the Ir $5d$ levels into the t_{2g} and the e_g bands. Then, SOC splits the degenerate t_{2g} levels in a lower $J_{\text{eff}} = 3/2$ quartet and an upper $J_{\text{eff}} = 1/2$ doublet. The ground state of the system is achieved placing the five electrons of the 4+ ionized Ir in a low-spin configuration, *i. e.* the $J_{\text{eff}} = 3/2$ band is full while the $J_{\text{eff}} = 1/2$ band is half-filled. This ground state is strictly reached only if a precise energetic requirement is fulfilled: $\Delta \ll \zeta \ll 10Dq$.

This work aimed to determine the cubic component $10Dq$ of the crystal field in Sr_2IrO_4 and $Sr_3Ir_2O_7$: indeed, experimental determinations of SOC ($\zeta \sim 0.4$ eV) and tetragonal crystal field ($\Delta \sim 0.1$ eV) have already been done. We utilized the spectroscopic technique of X-ray Raman scattering, which is a bulk sensitive and self-absorption free probe of the electronic structure of compounds with light elements. Soft XAS at the O K edge, hard XAS, RIXS and RXMS at the Ir $L_{2,3}$ edges can be used as well, but they are all affected by surface sensitivity and self-absorption issues and a clear picture of the electronic structure of these materials cannot be easily

extracted.

By exploiting the orientation dependence of the XRS cross-section and with the help of a single-ion model, we were able to assign each feature in the 528-535 eV energy loss range to a particular transition involving the Ir $5d$ states. This allowed us to obtain the values of the cubic crystal field splitting $10Dq = 3.8 \pm 0.82$ eV for Sr_2IrO_4 and 3.55 ± 0.13 eV for $Sr_3Ir_2O_7$. These values are very large when compared to SOC and the tetragonal crystal field. This implies that the e_g states are much higher in energy than the t_{2g} states and thus they do not contribute to the ground state wave function of the two iridates. The hierarchy of energies at play is therefore completely established experimentally and the implicit assumption of $\Delta \ll \zeta \ll 10Dq$ is validated.

From the measurements, we were also able to extract the energies of the electronic transitions: in particular, we found the value of the tetragonal crystal field splitting of the e_g states: 1.6 ± 0.82 eV in Sr_2IrO_4 and 1.9 ± 0.13 in $Sr_3Ir_2O_7$. Moreover, we found that the $3z^2 - r^2$ orbital is lower in energy than the $x^2 - y^2$, implying an elongation of the IrO_6 octahedra, as confirmed by structural studies of the two compounds.

To the best of our knowledge, ours are one of the first XRS measurements at the O K edge of transition metal oxides. Beside extracting quantitative informations on the electronic structure of iridates, we also demonstrate that XRS is a powerful and promising technique for the study of the electronic properties of these materials. We hope that this pioneering work will spark interest to study other transition metal oxides, with a special consideration to the much more examined high temperature cuprate superconductors, especially in extreme environments, such as high pressure, where other techniques (soft XAS in particular) cannot be performed.

Bibliography

[1] J. Bednorz and K. Müller, Zeitschrift für Physik B Condensed Matter **64**, 189 (1986).

[2] A. P. Ramirez, Journal of Physics: Condensed Matter **9**, 8171 (1997).

[3] G. Cao, J. Bolivar, S. McCall, J. E. Crow, and R. P. Guertin, Phys. Rev. B **57**, R11039 (1998).

[4] G. Cao, Y. Xin, C. S. Alexander, J. E. Crow, P. Schlottmann, M. K. Crawford, R. L. Harlow, and W. Marshall, Phys. Rev. B **66**, 214412 (2002).

[5] L. F. Mattheiss, Phys. Rev. B **13**, 2433 (1976).

[6] T. Mizokawa and A. Fujimori, Phys. Rev. B **54**, 5368 (1996).

[7] B. J. Kim, H. Jin, S. J. Moon, J.-Y. Kim, B.-G. Park, C. S. Leem, J. Yu, T. W. Noh, C. Kim, S.-J. Oh, J.-H. Park, V. Durairaj, G. Cao, and E. Rotenberg, Phys. Rev. Lett. **101**, 076402 (2008).

[8] S. J. Moon, H. Jin, K. W. Kim, W. S. Choi, Y. S. Lee, J. Yu, G. Cao, A. Sumi, H. Funakubo, C. Bernhard, and T. W. Noh, Phys. Rev. Lett. **101**, 226402 (2008).

[9] B. J. Kim, H. Ohsumi, T. Komesu, S. Sakai, T. Morita, H. Takagi, and T. Arima, Science **323**, 1329 (2009).

[10] D. Pesin and L. Balents, Nat. Phys. **6**, 376 (2010).

[11] F. Wang and T. Senthil, Phys. Rev. Lett. **106**, 136402 (2011).

[12] J. W. Kim, Y. Choi, J. Kim, J. F. Mitchell, G. Jackeli, M. Daghofer, J. van den Brink, G. Khaliullin, and B. J. Kim, Phys. Rev. Lett. **109**, 037204 (2012).

[13] H. Watanabe, T. Shirakawa, and S. Yunoki, Phys. Rev. Lett. **110**, 027002 (2013).

[14] R. Coldea, S. M. Hayden, G. Aeppli, T. G. Perring, C. D. Frost, T. E. Mason, S.-W. Cheong, and Z. Fisk, Phys. Rev. Lett. **86**, 5377 (2001).

[15] J. Kim, D. Casa, M. H. Upton, T. Gog, Y.-J. Kim, J. F. Mitchell, M. van Veenendaal, M. Daghofer, J. van den Brink, G. Khaliullin, and B. J. Kim, Phys. Rev. Lett. **108**, 177003 (2012).

[16] J. J. Randall, L. Katz, and R. Ward, Journal of the American Chemical Society **79**, 266 (1957).

[17] D. C. Johnston, J. P. Stokes, D. P. Goshorn, and J. T. Lewandowski, Phys. Rev. B **36**, 4007 (1987).

[18] S. Boseggia, H. C. Walker, J. Vale, R. Springell, Z. Feng, R. S. Perry, M. M. Sala, H. M. Rønnow, S. P. Collins, and D. F. McMorrow, Journal of Physics: Condensed Matter **25**, 422202 (2013).

[19] M. Moretti Sala, M. Rossi, S. Boseggia, J. Akimitsu, N. B. Brookes, M. Isobe, M. Minola, H. Okabe, H. M. Rønnow, L. Simonelli, D. F. McMorrow, and G. Monaco, Phys. Rev. B **89**, 121101 (2014).

[20] S. J. Moon, M. W. Kim, K. W. Kim, Y. S. Lee, J.-Y. Kim, J.-H. Park, B. J. Kim, S.-J. Oh, S. Nakatsuji, Y. Maeno, I. Nagai, S. I. Ikeda, G. Cao, and T. W. Noh, Phys. Rev. B **74**, 113104 (2006).

[21] H. J. Park, C. H. Sohn, D. W. Jeong, G. Cao, K. W. Kim, S. J. Moon, H. Jin, D.-Y. Cho, and T. W. Noh, Phys. Rev. B **89**, 155115 (2014).

[22] H. Gretarsson, J. Kim, D. Casa, T. Gog, K. R. Choi, S. W. Cheong, and Y.-J. Kim, Phys. Rev. B **84**, 125135 (2011).

[23] C. Liu, S.-Y. Xu, N. Alidoust, T.-R. Chang, H. Lin, C. Dhital, S. Khadka, M. Neupane, I. Belopolski, G. Landolt, H.-T. Jeng, R. Markiewicz, J. H. Dil, A. Bansil, S. D. Wilson, and M. Zahid Hasan, ArXiv e-prints (2014), arXiv:1403.2704 [cond-mat.str-el] .

[24] J. P. Clancy, A. Lupascu, H. Gretarsson, Z. Islam, Y. F. Hu, D. Casa, C. S. Nelson, S. C. LaMarra, G. Cao, and Y.-J. Kim, Phys. Rev. B **89**, 054409 (2014).

[25] S. Boseggia, R. Springell, H. C. Walker, A. T. Boothroyd, D. Prabhakaran, S. P. Collins, and D. F. McMorrow, Journal of Physics: Condensed Matter **24**, 312202 (2012).

[26] K. Ishii, I. Jarrige, M. Yoshida, K. Ikeuchi, J. Mizuki, K. Ohashi, T. Takayama, J. Matsuno, and H. Takagi, Phys. Rev. B **83**, 115121 (2011).

[27] X. Liu, V. M. Katukuri, L. Hozoi, W.-G. Yin, M. P. M. Dean, M. H. Upton, J. Kim, D. Casa, A. Said, T. Gog, T. F. Qi, G. Cao, A. M. Tsvelik, J. van den Brink, and J. P. Hill, Phys. Rev. Lett. **109**, 157401 (2012).

[28] M. Moretti Sala, S. Boseggia, D. F. McMorrow, and G. Monaco, Phys. Rev. Lett. **112**, 026403 (2014).

[29] M. Moretti Sala, K. Ohgushi, A. Al-Zein, Y. Hirata, G. Monaco, and M. Krisch, Phys. Rev. Lett. **112**, 176402 (2014).

[30] C. V. Raman, Indian Journal of Physics **2**, 387 (1928).

[31] G. Landsberg and L. Mandelstam, Naturwissenschaften **16**, 557 (1928).

[32] T. Suzuki, Journal of the Physical Society of Japan **22**, 1139 (1967).

[33] U. Bergmann, P. Glatzel, and S. P. Cramer, Microchemical Journal **71**, 221 (2002).

[34] S. Huotari, T. Pylkkänen, R. Verbeni, G. Monaco, and K. Hämäläinen, Nat. Mater. **10**, 489 (2011).

[35] M. W. Haverkort, A. Tanaka, L. H. Tjeng, and G. A. Sawatzky, Phys. Rev. Lett. **99**, 257401 (2007).

[36] Y. Mizuno and Y. Ohmura, Journal of the Physical Society of Japan **22**, 445 (1967).

[37] K. Tohji and Y. Udagawa, Phys. Rev. B **39**, 7590 (1989).

[38] W. Schülke, *Electron Dynamics by Inelastic X-Ray Scattering*, Oxford Series on Synchrotron Radiation (OUP Oxford, 2007).

[39] J. Kirz and D. Vaughan, *X-ray Data Booklet* (Lawrence Berkeley Laboratory, University of California, 1985).

[40] ESRF, "What is a synchrotron?" (2013), [Online; last modified 18-Jun-2013].

[41] N. Ashcroft and N. Mermin, *Solid state physics*, Science: Physics (Saunders College, 1976).

[42] O. Madelung, *Semiconductors: group IV elements and III-V compounds*, Data in science and technology (Springer-Verlag, 1991).

[43] J. Als-Nielsen and D. McMorrow, *Elements of Modern X-ray Physics* (Wiley, 2011).

[44] R. Verbeni, M. Kocsis, S. Huotari, M. Krisch, G. Monaco, F. Sette, and G. Vanko, Journal of Physics and Chemistry of Solids **66**, 2299 (2005).

[45] C. Ponchut, J. M. Rigal, J. Clément, E. Papillon, A. Homs, and S. Petitdemange, Journal of Instrumentation **6**, C01069 (2011).

[46] B. Beznosikov and K. Aleksandrov, Crystallography Reports **45**, 792 (2000).

[47] S. Boseggia, R. Springell, H. C. Walker, H. M. Rønnow, C. Rüegg, H. Okabe, M. Isobe, R. S. Perry, S. P. Collins, and D. F. McMorrow, Phys. Rev. Lett. **110**, 117207 (2013).

[48] S. Boseggia, R. Springell, H. C. Walker, A. T. Boothroyd, D. Prabhakaran, D. Wermeille, L. Bouchenoire, S. P. Collins, and D. F. McMorrow, Phys. Rev. B **85**, 184432 (2012).

[49] M. K. Crawford, M. A. Subramanian, R. L. Harlow, J. A. Fernandez-Baca, Z. R. Wang, and D. C. Johnston, Phys. Rev. B **49**, 9198 (1994).

[50] M. Subramanian, M. Crawford, and R. Harlow, Materials Research Bulletin **29**, 645 (1994).

[51] H. Matsuhata, I. Nagai, Y. Yoshida, S. Hara, S. ichi Ikeda, and N. Shirakawa, Journal of Solid State Chemistry **177**, 3776 (2004).

[52] M. Imada, A. Fujimori, and Y. Tokura, Rev. Mod. Phys. **70**, 1039 (1998).

[53] J. Hubbard, Proceedings of the Royal Society of London. Series A. Mathematical and Physical Sciences **276**, 238 (1963).

[54] G. Jackeli and G. Khaliullin, Phys. Rev. Lett. **102**, 017205 (2009).

[55] L. J. P. Ament, G. Khaliullin, and J. van den Brink, Phys. Rev. B **84**, 020403 (2011).

[56] Wikipedia, "Cubic harmonic — wikipedia, the free encyclopedia," (2014), [Online; accessed 16-April-2014].

[57] D. Griffiths, *Introduction to Quantum Mechanics* (Pearson Education, Limited, 2013).

[58] T. Willers, F. Strigari, N. Hiraoka, Y. Q. Cai, M. W. Haverkort, K.-D. Tsuei, Y. F. Liao, S. Seiro, C. Geibel, F. Steglich, L. H. Tjeng, and A. Severing, Phys. Rev. Lett. **109**, 046401 (2012).

[59] T. Mizokawa, L. H. Tjeng, G. A. Sawatzky, G. Ghiringhelli, O. Tjernberg, N. B. Brookes, H. Fukazawa, S. Nakatsuji, and Y. Maeno, Phys. Rev. Lett. **87**, 077202 (2001).

[60] J. C. Slater and G. F. Koster, Phys. Rev. **94**, 1498 (1954).

[61] W. Harrison, *Electronic structure and the properties of solids: the physics of the chemical bond*, Dover Books on Physics (Dover Publications, 1989).

[62] O. Andersen and O. Jepsen, Physica B+C **91**, 317 (1977).

[63] M. Schmidt, T. R. Cummins, M. Bürk, D. H. Lu, N. Nücker, S. Schuppler, and F. Lichtenberg, Phys. Rev. B **53**, R14761 (1996).

[64] Y. Bard, *Nonlinear parameter estimation* (Academic Press, 1974).

[65] I. Bersuker, *Electronic Structure and Properties of Transition Metal Compounds: Introduction to the Theory* (Wiley, 2010).

Acknowledgments

I am intensely grateful to most of the people I met in the past years. First of all, Prof. Giacomo Ghiringhelli, for his helpfulness and for the great opportunity he gave me to experience a trainee period at the ESRF, and Dr. Michael Krisch, for hosting me at beam line ID20 and for his proficiency and friendliness. I would particularly like to thank Dr. Marco Moretti, to whom I am deeply indebted for all he has done for me: his guidance, confidence and, above all, friendship. Thanks to the ID20 team: Ali, for his advices and (French) discussions, Christoph, for sharing wonderful stories about his worldwide travels, Roberto and Christian, for their willing and qualified support.

Thanks to all the people I met in Grenoble: if "a journey is best measured in friends rather than miles" (Tim Cahill), then I did find the right place.

Thanks to Giusy, who softened my comeback. Thanks to my parents, who supported me through everything I wanted to do and who urge me continually to do my best, as they do every day.

My heartfelt gratitude to all of you,
Matteo Rossi